Human Molecular Genetics, 2014, Vol. 23, No. 12 **3085–3101**
doi:10.1093/hmg/ddu013
Advance Access published on January 12, 2014

Induced ablation of *Bmp1* and *Tll1* produces osteogenesis imperfecta in mice

Alison M. Muir[1,2], Yinshi Ren[3], Delana Hopkins Butz[1], Nicholas A. Davis[1], Robert D. Blank[4,5,†], David E. Birk[6], Se-Jin Lee[7], David Rowe[8], Jian Q. Feng[3] and Daniel S. Greenspan[1,*]

[1]Department of Cell and Regenerative Biology, School of Medicine and Public Health, University of Wisconsin, Madison, WI, USA, [2]Laboratory of Genetics, University of Wisconsin, Madison, WI, USA, [3]Department of Biomedical Sciences, Baylor College of Dentistry Texas A&M Health Science Center, Dallas, TX, USA, [4]Geriatrics Research, Education, and Clinical Center, William S. Middleton Veterans Hospital, Madison, WI, USA, [5]Department of Medicine, Division of Endocrinology, Diabetes and Metabolism, School of Medicine and Public Health, University of Wisconsin, Madison, WI, USA, [6]Department of Pharmacology and Physiology, Morsani College of Medicine, University of South Florida, Tampa, FL, USA, [7]Department of Molecular Biology and Genetics, Johns Hopkins University School of Medicine, Baltimore, MD, USA and [8]Department of Reconstructive Sciences, Biomaterials and Skeletal Development, School of Dental Medicine, University of Connecticut, Farmington, CT, USA

Received September 23, 2013; Revised December 11, 2013; Accepted January 8, 2014

Osteogenesis imperfecta (OI), or brittle bone disease, is most often caused by dominant mutations in the collagen I genes *COL1A1*/*COL1A2*, whereas rarer recessive OI is often caused by mutations in genes encoding collagen I-interacting proteins. Recently, mutations in the gene for the proteinase bone morphogenetic 1 (BMP1) were reported in two recessive OI families. BMP1 and the closely related proteinase mammalian tolloid-like 1 (mTLL1) are co-expressed in various tissues, including bone, and have overlapping activities that include biosynthetic processing of procollagen precursors into mature collagen monomers. However, early lethality of *Bmp1*- and *Tll1*-null mice has precluded use of such models for careful study of *in vivo* roles of their protein products. Here we employ novel mouse strains with floxed *Bmp1* and *Tll1* alleles to induce postnatal, simultaneous ablation of the two genes, thus avoiding barriers of *Bmp1*$^{-/-}$ and *Tll1*$^{-/-}$ lethality and issues of functional redundancy. Bones of the conditionally null mice are dramatically weakened and brittle, with spontaneous fractures—defining features of OI. Additional skeletal features include osteomalacia, thinned/porous cortical bone, reduced processing of procollagen and dentin matrix protein 1, remarkably high bone turnover and defective osteocyte maturation that is accompanied by decreased expression of the osteocyte marker and Wnt-signaling inhibitor sclerostin, and by marked induction of canonical Wnt signaling. The novel animal model presented here provides new opportunities for in-depth analyses of *in vivo* roles of BMP1-like proteinases in bone and other tissues, and for their roles, and for possible therapeutic interventions, in OI.

INTRODUCTION

Osteogenesis imperfecta (OI) is a heritable connective tissue disorder characterized by deficits in bone material properties that result in bone fragility, and which can also result in low bone mass, bone deformities and impaired growth (1–3). More than 90% of OI cases are due to autosomal dominant mutations in *COL1A1* and *COL1A2*, the genes encoding the two chains of collagen I. Collagen I is by far the most abundant protein of bone, in which it is of major structural importance and serves as the template upon which mineral is deposited. Recently, recessive OI mutations have been reported in genes encoding the proteins FKBP65 and HSP47, which participate in proper intracellular procollagen folding; in the gene for PEDF, an

*To whom correspondence should be addressed at: Department of Cell and Regenerative Biology, School of Medicine and Public Health, University of Wisconsin, Room K4/430, Box 4672, 600 Highland Ave, Madison, WI 53792, USA. Tel: +1 6082624676; Email: dsgreens@wisc.edu
†Present address: Division of Endocrinology, Metabolism, and Clinical Nutrition, Medical College of Wisconsin, and Clement J. Zablocki VAMC, Milwaukee, WI, USA.

© The Author 2014. Published by Oxford University Press. All rights reserved.
For Permissions, please email: journals.permissions@oup.com

extracellular collagen I-binding protein and in genes encoding the three components of the collagen prolyl-3-hydroxylation complex (2,3).

Bone morphogenetic protein 1 (BMP1), the prototype of a group of structurally similar extracellular metalloproteinases that perform morphogenetic roles in a broad range of species (4,5), was first co-purified from bone extracts with the osteogenic TGFβ-like factors BMPs 2 and 4 (6). BMP1 and related proteinases were later shown to be capable of activating BMPs 2/4 by cleaving the extracellular antagonist chordin (Chd), in the context of embryonic dorsoventral patterning, in which BMPs 2/4 are major ventralizing proteins (7–9). Surprisingly, despite its initial inferred relationships with BMPs 2/4, the first demonstrated role for BMP1 was as a procollagen C-proteinase (pCP) (10), responsible for the biosynthetic cleavage of C-propeptides from procollagen precursors of the major fibrillar collagens I–III, a step necessary for the production of mature collagen monomers. Roles for BMP1-like proteinases in bone biology have thus been inferred by its association with osteoinductive factors BMPs 2/4, its demonstrated pCP activity; and such roles have also been inferred by findings of mutations at the procollagen I C-propeptide cleavage site that result in decreased cleavage efficiency, in cases of dominant OI (11). More recently, exome sequencing has identified the *BMP1* gene as a candidate locus in two families with recessive OI (12,13).

There are four mammalian BMP1-like proteinases: BMP1 and mTLD (mammalian tolloid), which are encoded by alternatively spliced mRNAs from the same gene, and mTLL (mammalian tolloid-like) 1 and 2, which are each genetically distinct. In addition to providing pCP activity and activating BMP2/4, BMP1-like proteinases are reported to biosynthetically process various precursors into functional proteins involved in forming the extracellular matrix (ECM), and to activate additional growth factors (4,5). BMP1-like proteinase activities relevant to bone biology include activation of lysyl oxidase (an enzyme necessary to covalent cross-link formation in collagen fibrils) (14), biosynthetic processing of biglycan, osteoglycin and collagen V (all of which are thought to participate in regulating collagen I fibrillogenesis) (15), cleavage of dentin matrix protein 1 (DMP1) to produce peptides involved in ECM mineralization and osteocyte maturation (16,17) and activation of TGFβ1 (18), a critical protein in bone biology (19,20).

Mice null for the *Bmp1* gene, which encodes both BMP1 and mTLD, are perinatal lethal from defects that include failure to close the ventral body wall (21). However, although *Bmp1*$^{-/-}$ embryos contain abnormal collagen fibrils, axial and appendicular skeletal elements are grossly normal, and only mild developmental delay in membranous bones of the skull is observed (21). Mice null for the mTLL1 gene (*Tll1*) are embryonic lethal at 13.5-dpc owing to cardiovascular defects, with no apparent defects in collagen fibrils (22), despite the finding that *Tll1* is responsible for residual pCP activity in *Bmp1*$^{-/-}$ embryo fibroblasts (23). Early lethality has precluded further study of *Bmp1*$^{-/-}$ and *Tll1*$^{-/-}$ *in vivo* roles in bones and other tissues.

Tll1 and *Bmp1* are co-expressed in various tissues, including bone (22,24–26), and have been shown to be additive/redundant in provision of cleavage activities against Chd, probiglycan and procollagen I in mouse embryo fibroblast (MEF) cultures (15,23). Overlapping/redundant activities may thus help explain the grossly normal skeletal morphology of *Bmp1*$^{-/-}$ embryos, and apparently normal collagen fibrils in *Tll1*$^{-/-}$ embryos. In contrast to *Bmp1* and *Tll1*, the mTLL2 gene (*Tll2*) is expressed in developing skeletal muscle, but not bone (24), and *Tll2*-null mice present with only a mild muscle phenotype (27). Additionally, mTLL2 shows absent or reduced levels of activity against many ECM-related substrates [e.g. (16,23,24)]. Thus, it is unlikely that mTLL2 plays a major role in bone biology.

Here, we employ novel mouse strains with floxed *Bmp1* and *Tll1* alleles for induced postnatal, simultaneous ablation of the two genes, thus avoiding the barriers of *Bmp1*$^{-/-}$ and *Tll1*$^{-/-}$ lethality and issues of functional redundancy. In addition, a recent report that mTLD is a component of human plasma and may be involved in bone fracture repair (28) raised the potential issue that phenotypic effects of a tissue-specific knockdown of *Bmp1* and/or *Tll1* might to some extent be masked/compensated for by activities of circulating mTLD-related proteins. Thus, ubiquitous *Bmp1* and *Tll1* knockdown in all tissues was employed. The presented data demonstrate *Bmp1*/*Tll1* products to be of profound importance to bone growth and modeling in mammals.

RESULTS

Creation of mice with ubiquitous knockdown of the *Bmp1* and *Tll1* genes

Toward conditional knockdown of the *Tll1* gene, a mouse strain was produced with a floxed *Tll1* allele, such that excision with Cre results in removal of exon 6 sequences that include the Zn^{2+}-binding active site (Fig. 1A) and a frame shift, such that 20 amino acids downstream of the shift are translated in the new frame prior to a premature stop codon. Thus, the resulting deleted exon 6 allele (*Tll1*$^{\Delta 6}$) is essentially null, producing either a severely truncated product comprising only 64 amino acid residues of mTLL1 that, in light of numerous structure-function studies performed on this family of proteinases, would be unlikely to interact with substrates, or an RNA with a premature stop codon that is rapidly degraded via nonsense-mediated decay. A mouse strain was produced with a floxed *Bmp1* allele (Fig. 1E), such that excision with Cre results in removal of exons 3–6, thus removing sequences encoding the prodomain–protease domain junction and the majority of the protease domain, including the Zn^{2+}-binding active site (all of which are shared by BMP1 and mTLD) and a frame shift, to create a null allele (*Bmp1*$^{\Delta 3-6}$) in which either an extremely truncated protein containing only a few prodomain sequences is produced or in which RNA with premature stop codon is rapidly degraded via nonsense-mediated decay.

The *neo*^{r} cassette was removed from floxed *Tll1* alleles (Fig. 1A and C), and crosses were performed to produce mice doubly homozygous for the floxed *Bmp1* and *Tll1* alleles and hemizygous for a Cre-ERT2 fusion transgene driven by the human ubiquitin C promoter (29), for ubiquitous Cre activity upon treatment of mice with tamoxifen. Mice were administered tamoxifen for 6 days at 4 weeks of age, and for another 6 days at 6 weeks of age, to optimize excision rates and, no sooner than 3 weeks after completion of tamoxifen treatment, genomic DNA from ear punch samples were screened via PCR (Fig. 1F), and only mice showing >75% excision in the *Bmp1*^{floxed} allele (97% of all tamoxifen-treated mice screened) were subjected to further analysis. Subsequent RT-PCR analysis of RNA from

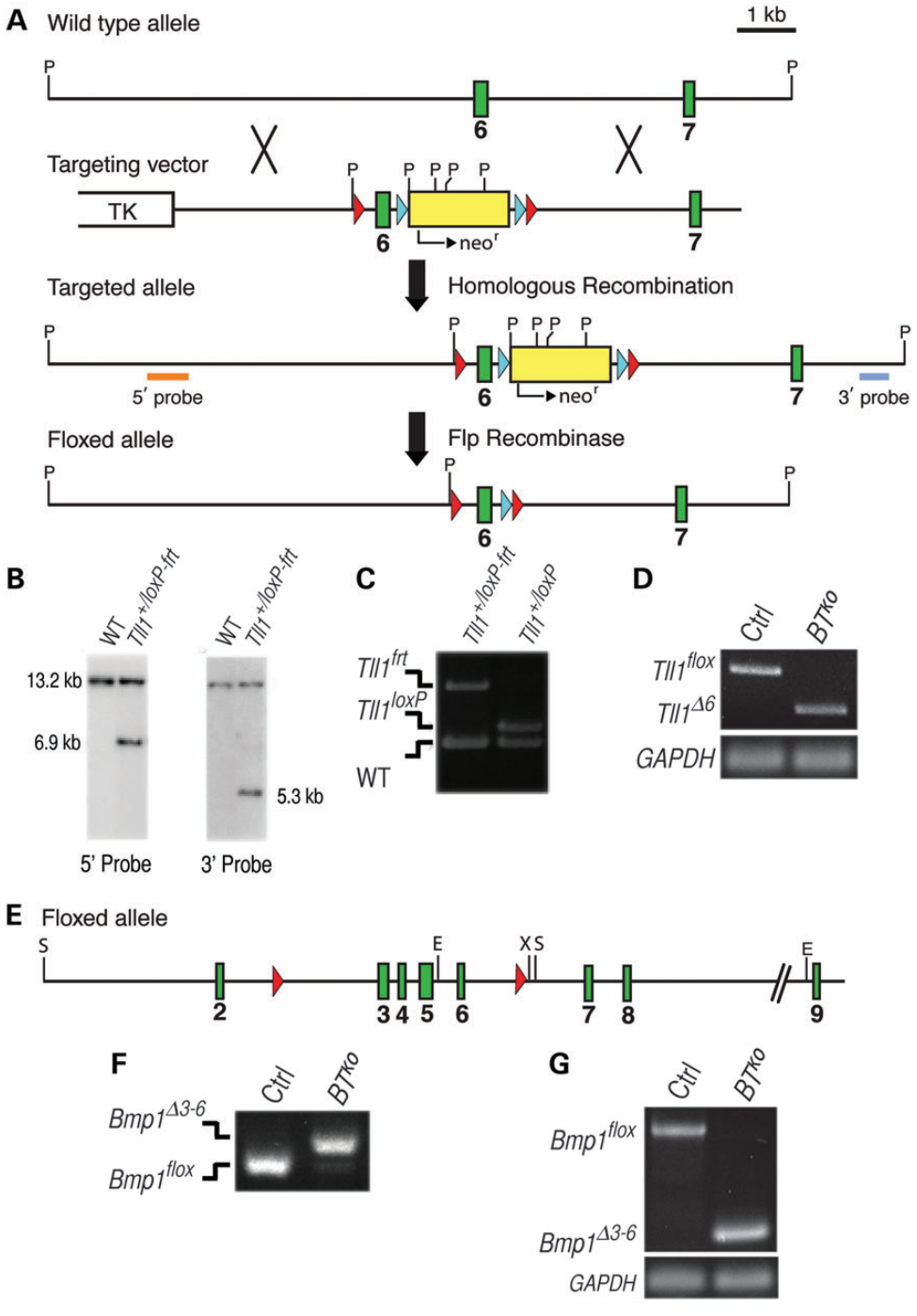

Figure 1. Conditional disruption of *Tll1* and *Bmp1*. (**A**) Structure of targeting vector and *Tll1* locus before and after homologous recombination and subsequent Flp- and Cre-induced recombination to produce alleles $Tll1^{loxP}$ and $Tll1^{\Delta 6}$, respectively. Arrows indicate directionality for transcription of neo^r (yellow box). Open box, TK selection gene. Green boxes represent *Tll1* exons. *Frt* and *loxP* sequences are indicated by blue and red arrowheads, respectively. P, PstI. Orange and blue boxes represent 1.1-kb Eco72I-NheI and 496-bp HpaI-PstI 5′ and 3′ external Southern blot probes, respectively. (**B**) Genomic Southern blot analysis of PstI-restricted DNA from wild-type (WT) or correctly targeted ($Tll1^{+/loxP-frt}$) ES clones. The 5′ probe detected 13.2-kb and 6.9-kb bands from wild-type and targeted alleles, respectively. The 3′ probe detected the 13.2-kb wild-type allele band, and a 5.3-kb band corresponding to the targeted allele. (**C**) Excision of the flrted neomycin resistance cassette. PCR genotyping of tail genomic DNA from mice heterozygous for the $Tll1^{loxP-frt}$-targeted allele, and from mice heterozygous for the $Tll1^{loxp}$ allele, from which the flrted neo^r cassette has been excised via crossing with the ACTB:FLPe line of Flp 'deleter' mice. Bands of 663, 770 and 1130 bp correspond to wild type, $Tll1^{loxP}$ and $Tll1^{loxP-frt}$ alleles, respectively. (**D**) RT–PCR of total RNA from femora shows tamoxifen-induced excision of floxed *Tll1* sequences. Bands of 179 and 544 bp correspond to $Tll^{\Delta 6}$ (excised) and Tll^{flox} (unexcised control) alleles, respectively. (**E**) Green boxes and red arrowheads represent *Bmp1* exons and *LoxP* sites, respectively, in floxed *Bmp1* allele. (**F**) Screening of tamoxifen-induced excision of floxed alleles using PCR genotyping of ear genomic DNA shows extent of tamoxifen-induced excision of floxed *Bmp1* sequences from a BT^{KO} mouse. Bands of 233 and 298 bp correspond to $Bmp1^{flox}$ (unexcised) and $Bmp1^{\Delta 3-6}$ (excised) alleles, respectively. BT^{KO} mice with $<75\%$ excision were excluded from further study. (**G**) RT–PCR of total RNA from femora shows tamoxifen-induced excision of floxed *Bmp1* sequences. Bands of 243 and 811 bp correspond to $Bmp1^{\Delta 3-6}$ (excised) and $Bmp1^{flox}$ (unexcised control) alleles, respectively.

femora of these mice showed them to be doubly homozygous for excised *Bmp1* and *Tll1* alleles (BT^{KO} mice), with un-excised, floxed *Bmp1* and *Tll1* sequences undetectable (Figs 1D and 2G), consistent with the conclusion that particularly high excision rates are achieved in BT^{KO} bone.

BT^{KO} mice are reduced in size and have bones with enlarged entheses and spontaneous fractures

Subsequent to tamoxifen-induced excision of *Bmp1* and *Tll1* sequences, BT^{KO} mice show reduced weight gain compared with control littermates (Fig. 2), so that by 17 weeks of age (11 weeks after the final tamoxifen injection), they are significantly smaller, with an average weight 73% of control. Some of the difference in weight is due to a reduction in adipose tissue (Supplementary Material, Fig. S1), but BT^{KO} mice also have a 13% reduction in length and a 5% reduction in femur length (Fig. 2), thus indicating impairment of skeletal growth. Other observed skeletal manifestations of the BT^{KO} phenotype included bony protuberances found on numerous bones upon initial dissections of BT^{KO} mice. To obtain a global view of the distribution of these abnormalities, complete skeletons of a small number of BT^{KO} and control mice ($n = 2$, each) were cleared of soft tissues via Dermestid beetles. The bony protuberances were found on BT^{KO} scapulae, long bones and pelvises (Fig. 3A–C) and corresponded to enlarged entheses, at which tendons and ligaments attach to bone. In addition, deformation of the pelvis was observed in the BT^{KO} skeletons (Fig. 3C), as were calluses on ribs (Fig. 3D), some of which still contained cartilaginous cores (Fig. 3E), apparently marking sites of healing of spontaneous fractures.

Spontaneous fractures such as those seen in BT^{KO} ribs can result from mild trauma and/or muscle contraction and are suggestive of profoundly weakened bone. Enlarged entheses can result from cycles of muscle contraction and relaxation that are accompanied by cycles of microfracturing and healing of bone at insertion sites, again consistent with the possibility of severely weakened bone. We note that mice null for the gene for myostatin (GDF8), an inhibitor of skeletal muscle growth that has been proposed to be activated by BMP1-like proteinases (30), have a doubling of skeletal muscle mass that is accompanied by enlarged entheses, thought to occur to accommodate the enlarged tendons at muscle attachment sites (31). However, we found BT^{KO} muscle mass to be reduced compared with that of controls, proportionate to the reduced mass of the mice themselves (Supplementary Material, Fig. S2). Thus, if proteolytic activation of myostatin is decreased in BT^{KO} mice, it is not affected to an extent sufficient to affect muscle mass, perhaps due in part to expression of the BMP1-like proteinase mTLL2 in skeletal muscle (24). We thus conclude spontaneous fractures

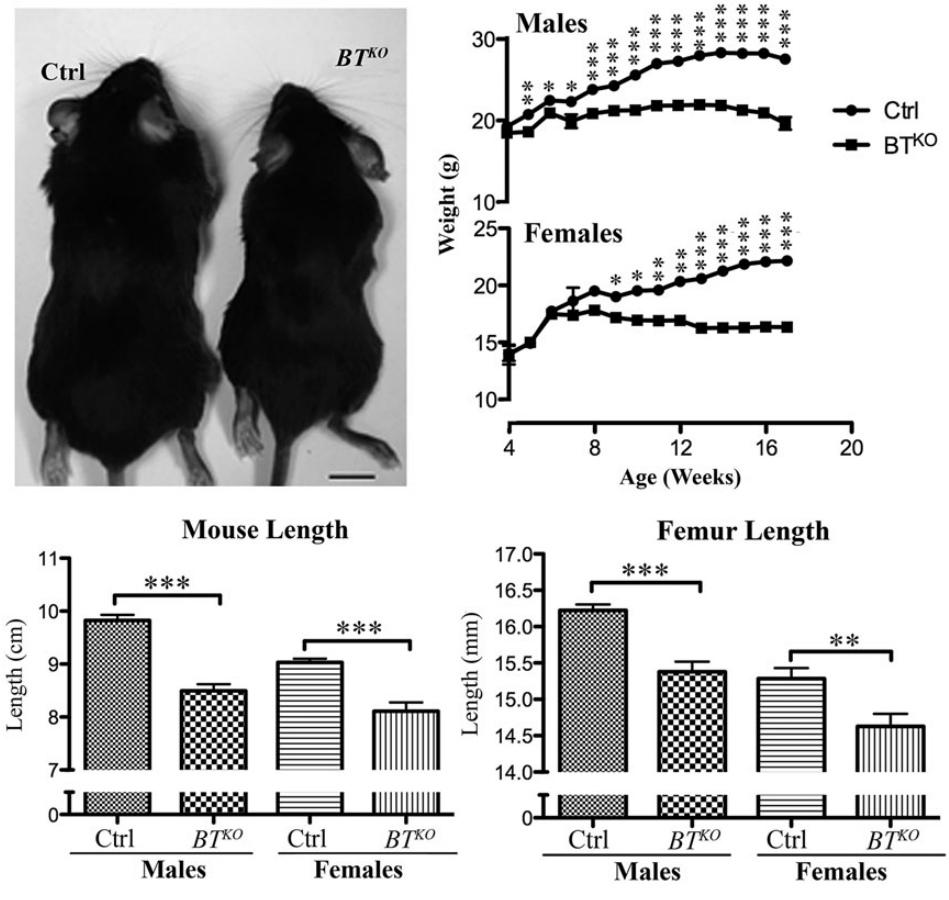

Figure 2. BT^{KO} mice are runted compared with control littermates. (Top left) Representative image of control (Ctrl) and BT^{KO} mice at 17 weeks of age. (Top right) Mice (male controls, $n = 13$; all others, $n = 10$) were weighed weekly, and both total body length (nose to anus) (bottom left) and femur length (bottom right) of the same animals were measured upon sacrificing. *P*-values: $^{*} < 0.05$, $^{**} < 0.01$, $^{***} < 0.001$.

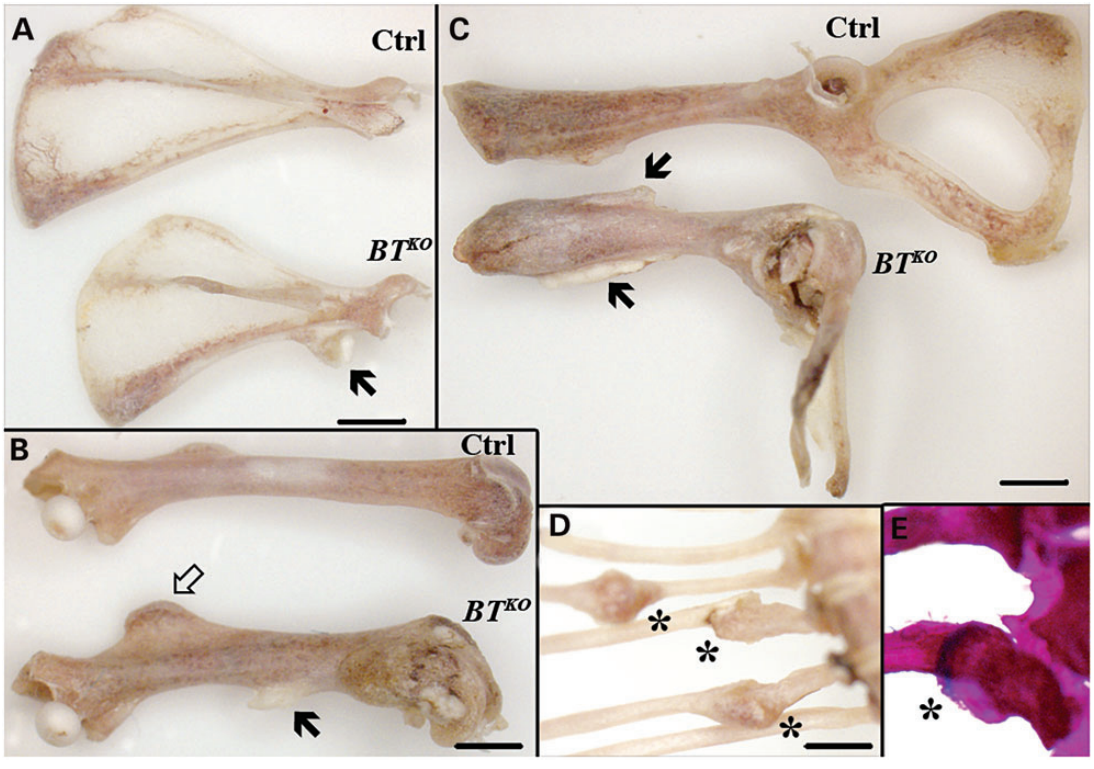

Figure 3. Enlarged entheses and spontaneous fractures in BT^{KO} mice. Representative images of scapula (**A**), femur (**B**) and pelvis (**C**) of control (Ctrl) and BT^{KO} mice at 17 weeks of age cleaned by Dermestid beetles. Enlarged entheses of BT^{KO} mice are indicated by black arrows. In particular, note the enlargement of the third trochanter (arrow outline), the attachment site for the ascending tendon of the gluteus maximus muscle, on the BT^{KO} femur (B), and the 90° distortion of the BT^{KO} pelvis (C). Calluses are marked (asterisks) on the ribs of a BT^{KO} mouse (**D**). Alizarin red/alcian blue staining of BT^{KO} ribs found the presence of blue, cartilaginous cores in some calluses (**E**), indicating that they were the sites of spontaneous fracturing of the ribs. Scale bars: 2 mm.

and enlarged entheses to be due to substantially weakened bone, without contribution from enlargement or strengthening of skeletal muscle. As in the case of the enlarged entheses, it seems likely that the deformed pelvises may result from cycles of microfracturing and healing in response to cycles of muscle contraction and relaxation. Interestingly, enlarged entheses, a prominent feature of BT^{KO} bones, have been shown in a hypomineralized phenotype resulting from loss of DMP1 (17), consistent with the possibility that enlarged BT^{KO} entheses may result, at least in part, from the hypomineralization attendant upon decreased DMP1 cleavage.

BT^{KO} femora have increased brittleness and decreased strength and stiffness

To determine the whole bone biomechanical characteristics of BT^{KO} mice, both femora from 10 BT^{KO} and 13 control males, and from 10 each BT^{KO} and control females were subjected to three-point bending analysis. As can be seen from Figure 4, total displacement, the total amount of bone deformation prior to fracture, was markedly reduced in BT^{KO} femora, as was post-yield displacement, a measure of ductility, thus showing BT^{KO} femora to be significantly more brittle than controls. Maximum load sustained prior to fracture was also markedly reduced in BT^{KO} femora, as was the energy necessary to fracture BT^{KO} femora, measured as the area under the load-displacement curve. Thus, BT^{KO} femora are shown to be more brittle and weaker and capable of absorbing less energy than those of controls, definitive characteristics of OI. Whole bone stiffness and yield load, the force necessary to cause permanent bone damage, were also significantly reduced in BT^{KO} bone (Supplementary Material, Table S1). Representative load-displacement curves for control and BT^{KO} demonstrate the almost total lack of post-yield displacement (ductility) prior to fracture in BT^{KO} femora (Fig. 4).

Following fracture, specimen geometry in the plane of the fracture was assessed (see Materials and methods), allowing calculation of corresponding tissue-level mechanical properties, using standard beam equations (32,33). Calculated tissue-level properties (Supplementary Material, Table S1), which provide the material properties of the bone independent of size and shape, provided supporting evidence that BT^{KO} femora are more brittle and weaker than controls. Values demonstrated a lower Young's modulus and post-yield strain for BT^{KO} femora compared with controls, suggestive of inferior material properties for BT^{KO} bone, with deficits in mineralization and bone ECM protein components, respectively; lowered toughness and yield stress (predicted strength) indicative of lower inherent resistance to fracture and lower bending strength, respectively; and lower maximum stress capable of causing fracture. The demonstrated impairment of strength, stiffness, post-yield displacement and energy to failure in BT^{KO} femora represents a global deficit in biomechanical performance, affecting all its major elements.

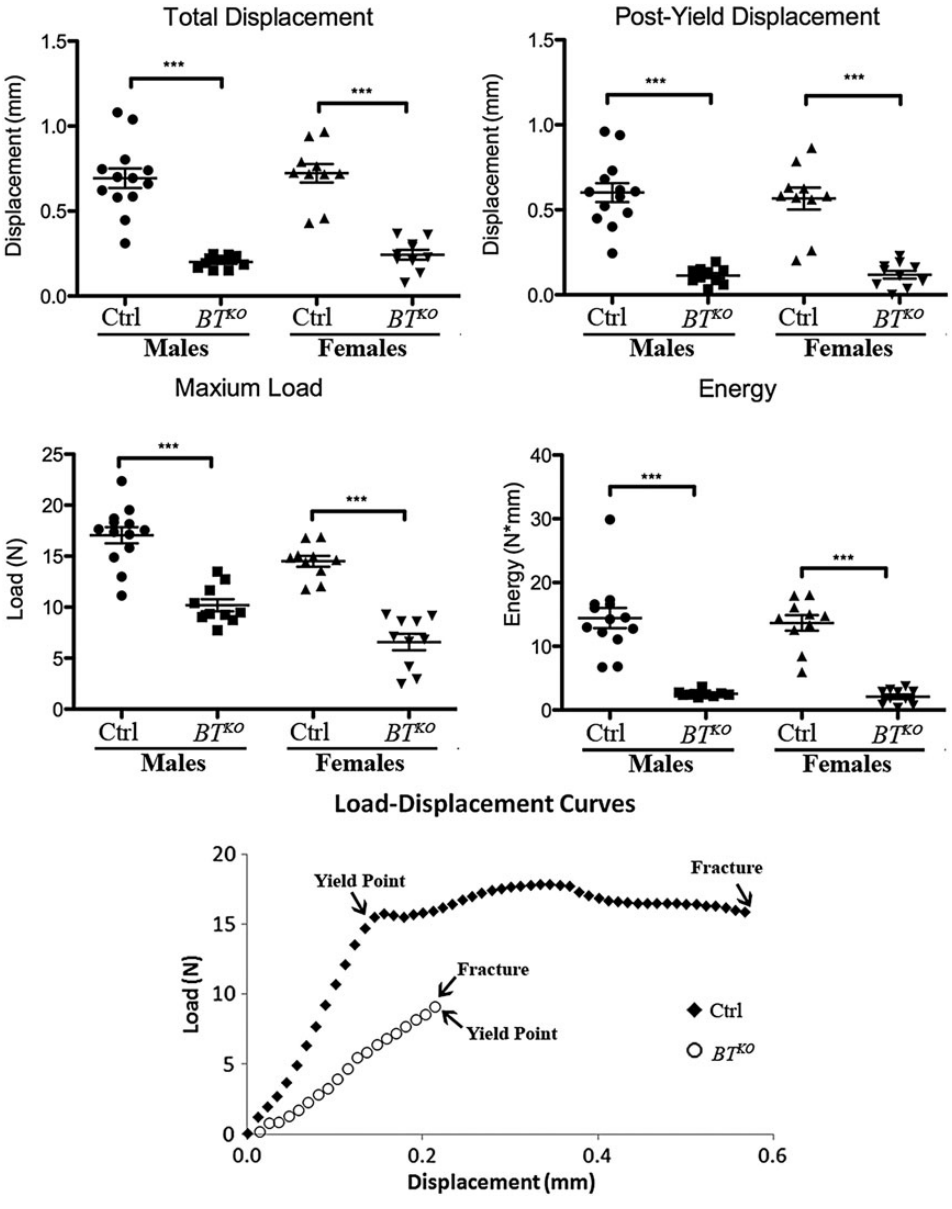

Figure 4. Whole bone mechanical performance comparison of BT^{KO} and wild-type femora. Three-point bending analysis was performed on femora from 10 BT^{KO} and 13 control males, and from 10 each BT^{KO} and control females. Both femora from each animal were tested, and the averaged value taken as the femoral biomechanical performance for that mouse. *P*-values: $^{*} < 0.05$, $^{**} < 0.01$, $^{***} < 0.001$. Representative load-displacement curves for control and BT^{KO} femora are shown. Yield points mark the beginnings of plastic deformation of bones.

Radiography and high-resolution microcomputed tomography

X-rayed BT^{KO} femora showed signs of spontaneous fractures, thinned cortical bone, increased amounts of trabecular bone and, in some cases, flaring of the distal femur (Fig. 5A). In some BT^{KO} mice, flaring of the proximal tibia was also seen (Supplementary Material, Fig. S3). This type of deformation of metaphyseal regions is suggestive of a softening of the bones owing to mineralization defects, although no bowing of diaphyseal regions was observed. Although only a small number of metaphyses were flared to the extent shown in Fig. 5A and Supplementary Material, Fig. S3, ~2/3 of BT^{KO} distal femora were observed to have some degree of flaring. Radiography also showed BT^{KO} mice to have pronounced kyphosis at 4 months of age, which became even more severe at 6 months of age (Fig. 5B), characteristics that can be found in OI, osteoporosis or ligamentous disease.

Analysis by microcomputed tomography (μ-CT) of BT^{KO} and control femoral diaphyses (Fig. 5C) showed BT^{KO} femora to have significantly smaller total volume (TV) and bone volume (BV), thus confirming the BT^{KO} cortical bone in this region to be thinner than that of controls, whereas the reduced BV/TV ratio showed the BT^{KO} diaphyseal cortical bone to have increased porosity as well. The same analysis also showed BT^{KO} cortical bone to have reduced tissue mineral density compared with control bone. Analysis by μ-CT of metaphyses again

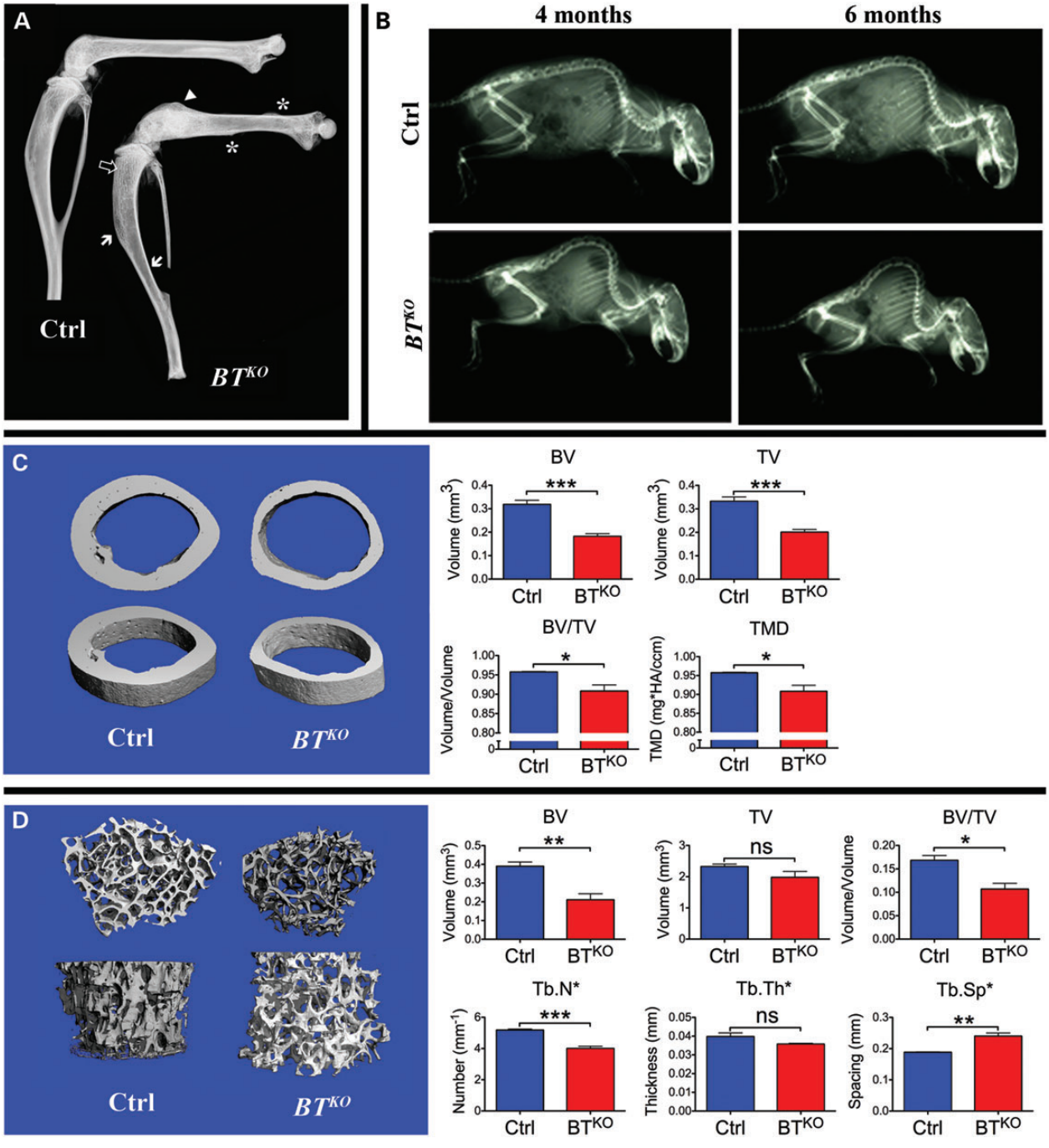

Figure 5. Radiography and high-resolution μ-CT comparisons of BT^{KO} and control bone. (**A**) X-rayed hindlimbs show calluses at the sites of spontaneous fractures (asterisks), flaring of the distal femur (arrowhead), highly thinned cortical bone (white arrows) and increased trabecular bone (outlined arrow) in a representative BT^{KO} specimen. (**B**) Radiography of four representative mice shows 4-month-old BT^{KO} mice to have kyphosis and shows the kyphosis to become considerably more pronounced at 6 weeks of age. The individuals shown are female. (**C**) Representative μ-CT images of femoral diaphyses show BT^{KO} cortical bone to have smaller total volume (TV) and bone volume (BV), increased porosity (BV/TV) and reduced tissue mineral density (TMD), compared with controls. Quantitation of the data is shown in histogram form (blue, controls; red, BT^{KO}). (**D**) Representative μ-CT images of femoral metaphyses show lowered BV, BV/TV, reduced Tb.N and increased tracecular spacing (Tb.Sp), (but no significant difference in Tb.Th or TV) in BT^{KO} trabecular bone, compared with controls. Quantitation of the data is shown in histogram form (blue, controls; red, BT^{KO}). *P*-values: $^{*}< 0.05$, $^{**}< 0.01$, $^{***}< 0.001$. ns, not significant.

showed a lowered BT^{KO} BV/TV ratio and also showed reduced trabecular bone number (Tb.N) and increased trabecular spacing (Tb.Sp) (Fig. 5D). The thin, porous cortical bone and reduced Tb.N and increased Tb.Sp of BT^{KO} bone are, together, somewhat reminiscent of the same features observed in osteoporotic bone.

Dynamic histomorphometry

Sequential *in vivo* incorporation of fluorochromes calcein and alizarin red into newly calcifying bone showed the labeling surface (LS/BS, bone surfaces containing calcein, alizarin red or both) of BT^{KO} mice to be much greater than those of controls, and the same is true for mineralizing surface [MS/BS, bone surfaces containing both calcein and alizarin + $\frac{1}{2}$(surfaces containing either calcein or alizarin) the extent of bone surface that is actively mineralizing] (Table 1). A representative image illustrative of the difference in calcein and alizarin red incorporation into BT^{KO} and control bone is shown in Figure 6A. There is no difference in mineral apposition rate (MAR, the distance between calcein and alizarin red labels divided by time between the labels) between BT^{KO} and control bone; however, the bone formation rate (BFR, MAR × MS/BS) is seen to be twice that in BT^{KO} bone as in control bone (Table 1). As the MAR is a measure of the rate of ECM deposition per osteoblast, whereas the BFR multiplies this rate by the fraction of bone surface with active osteoblasts (MS/BS, thus providing insights into the numbers of osteoblasts actively depositing ECM), it is apparent that there are much greater numbers of osteoblasts depositing mineralizing ECM within BT^{KO} bone than in control bone.

Table 1. Quantitative histomorphometry of mouse femur

	Ctrl	BT^{KO}	*P*-value
Dynamic histomorphometry			
LS/BS	26.90 ± 8.12	42.32 ± 1.80	0.004
MS/BS	14.83 ± 4.57	24.77 ± 1.63	0.001
MAR	0.76 ± 0.12	0.85 ± 0.24	ns
BFR	0.11 ± 0.04	0.22 ± 0.07	0.004
Osteoblast activity			
AP/BS	49.76 ± 10.62	42.56 ± 2.46	ns
AP_L/AP	32.75 ± 8.52	47.8 ± 5.47	0.003
AP_NL/AP	62.22 ± 9.38	44.43 ± 6.11	0.002
Osteoclast activity			
TRAP/BS	1.84 ± 1.73	5.73 ± 3.68	0.022
TRAP_R/BS	0.54 ± 0.67	2.13 ± 1.53	0.026
TRAP_Only/BS	1.18 ± 1.25	2.04 ± 1.43	ns

Cellular abnormalities of BT^{KO} bone

Interestingly, although staining for alkaline phosphatase (AP), a marker for active osteoblasts and quiescent bone lining cells on bone surfaces (AP/BS), was similar for BT^{KO} and control bone, the proportion of active osteoblasts lining labeling surfaces (AP_L/AP), at which mineral is being deposited, was markedly increased in BT^{KO} bone compared with controls, whereas the proportion of inactive osteoblasts lining non-labeling surfaces (AP_NL/AP) was markedly decreased in BT^{KO} bone compared with controls (Table 1). Thus, increased numbers of active osteoblasts, rather than increased numbers of total osteoblasts, are shown to be responsible for the much greater deposition rate of mineralizing ECM detected by dynamic histomorphometry.

Staining for tartrate-resistant acid phosphatase (TRAP), a marker for osteoclasts, showed a sharp increase in numbers of osteoclasts lining bone surfaces (TRAP/BS) in both BT^{KO} trabecular and cortical bone (Table 1), as show in Figure 6B. Whereas numbers of osteoclasts adjacent to non-mineralizing surfaces (TRAP_Only/BS) were not significantly higher in BT^{KO} than in control bone, osteoclasts adjacent to mineralizing surfaces (TRAP_R/BS) were ~4-fold greater in BT^{KO} than in control bone (Table 1). Thus, the

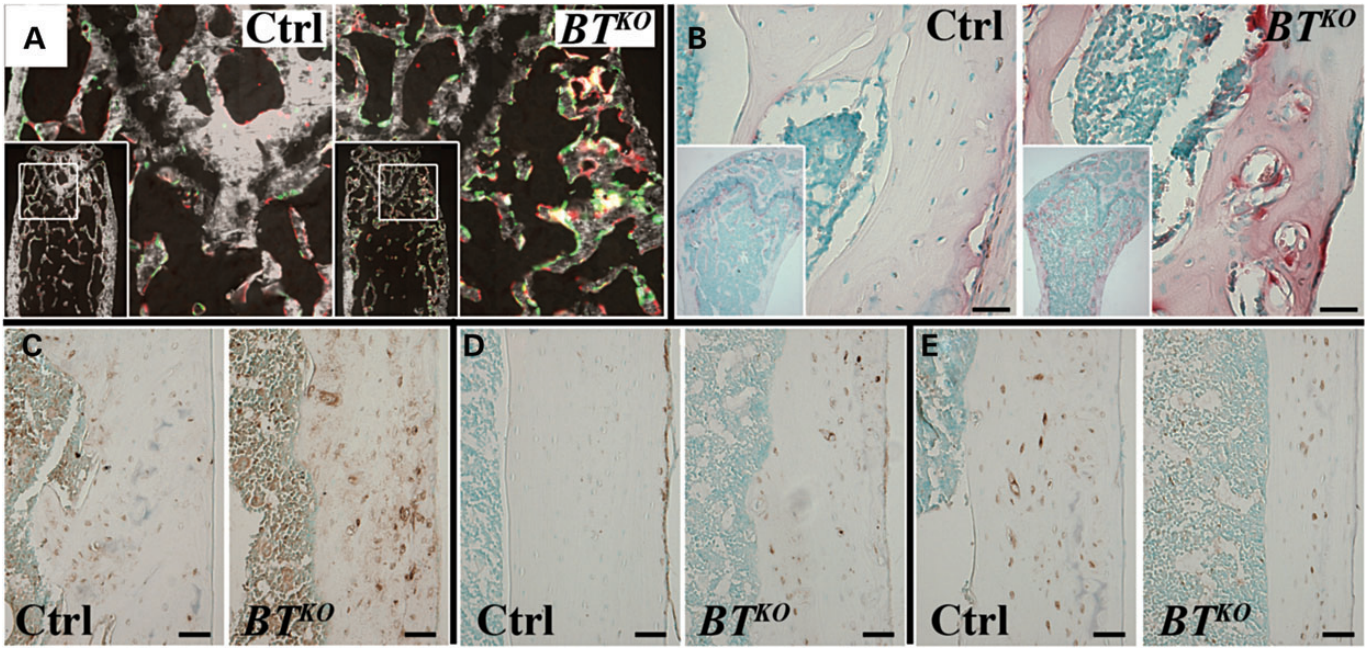

Figure 6. Dynamic histomorphometric differences and cellular abnormalities in BT^{KO} long bones. (**A**) *In vivo* double fluorochrome labeling with calcein (green) and alizarin red shows greatly increased labeled bone surfaces in the trabecular portion of BT^{KO} femur, compared with a control. (**B**) TRAP staining for osteoclasts (red) is sharply increased in BT^{KO} bone, compared with control, as shown in trabecular portions of the femur. Immunohistochemical staining (brown) performed on cortical femur showed higher levels of MEPE (**C**) and E-11 (**D**), and lower levels of sclerostin (**E**) for BT^{KO} bone than those for controls. Scale bars: 50 μm.

increased numbers of osteoblasts at mineralizing surfaces are amply matched by increased numbers of osteoclasts, explaining how, despite an elevated BFR indicative of increased numbers of active osteoblasts, BT^{KO} cortical bone is thinner and there are decreased Tb.N and increased inter-trabecular spacing (Tb.Sp) in BT^{KO} owing to resorption.

Immunohistochemical staining for MEPE (matrix extracellular phosphoglycoprotein, expressed in both osteoblasts and osteocytes) (Fig. 6C) and E-11/gp38 (a marker of early osteocytes) (Fig. 6D) was increased in the lacunae of BT^{KO} cortical bone, compared with controls, whereas staining for sclerostin, a marker of mature osteocytes (Fig. 6E), seemed somewhat decreased in BT^{KO} bone. These results suggest a deficit in osteocyte maturation and are somewhat reminiscent of similar results observed in DMP1-null mice (34), consistent with the possibility that part of the BT^{KO} bone phenotype may result from decreased proteolytic activation of DMP1.

To further examine possible derangements of BT^{KO} osteocytes, staining was performed with FITC, a small-molecular-weight dye that permeates the non-mineralized spaces in bone, thus providing a visual representation of the organization of non-mineralized cells, cellular processes and fibers under the confocal microscope. As can be seen from Figure 7A, BT^{KO} osteocytes showed a relative loss of dendritic processes, by which mature osteocytes communicate with one another, receive mechanosensory signals and participate in the regulation of bone turnover (35); and a fraction of BT^{KO} osteocytes seemed unable to maintain the integrity of the lacunae in which they were located, resulting in penetration of FITC through lacunae walls (Supplementary Material, Fig. S4).

Backscattered scanning electron microscopy (SEM) contrasted the homogeneous distribution of mineral in control bone with a heterogeneous distribution of areas of higher and lower levels of mineral in BT^{KO} bone (Fig. 7B). It also showed lacunae to be more rounded, less spindle-shaped and larger in BT^{KO} than in control bone, consistent with a maturation defect in BT^{KO} osteocytes. Acid-etched, resin-casted SEM images showed the malformed BT^{KO} osteocytes and lesser numbers of dendrites in greater detail (Fig. 7C).

Goldner's Masson trichrome staining of cortical bone shows BT^{KO} cortical bone to contain seams of unmineralized osteoid (Fig. 7D), which can also be seen via acid-etched SEM (Fig. 7C), another indication of a deficit in osteocyte function. Thus, a BT^{KO} osteocyte maturation defect is supported by (1) increased osteoid seams, (2) enlarged osteocyte cell bodies, changes in cell shape, reduced numbers of dendrites and changes to the lacunar-canalicular system and (3) gene expression pattern changes.

Interestingly, another consistent cellular change noted in BT^{KO} bone was a large increase in the numbers of adipocytes in the marrow (Fig. 7E). While it is not clear the extent to which this cellular change might contribute to the bone phenotype, it suggests the possibility of further derangements in cell differentiation pathways owing to loss of BMP1-like proteinase activity in BT^{KO} mice.

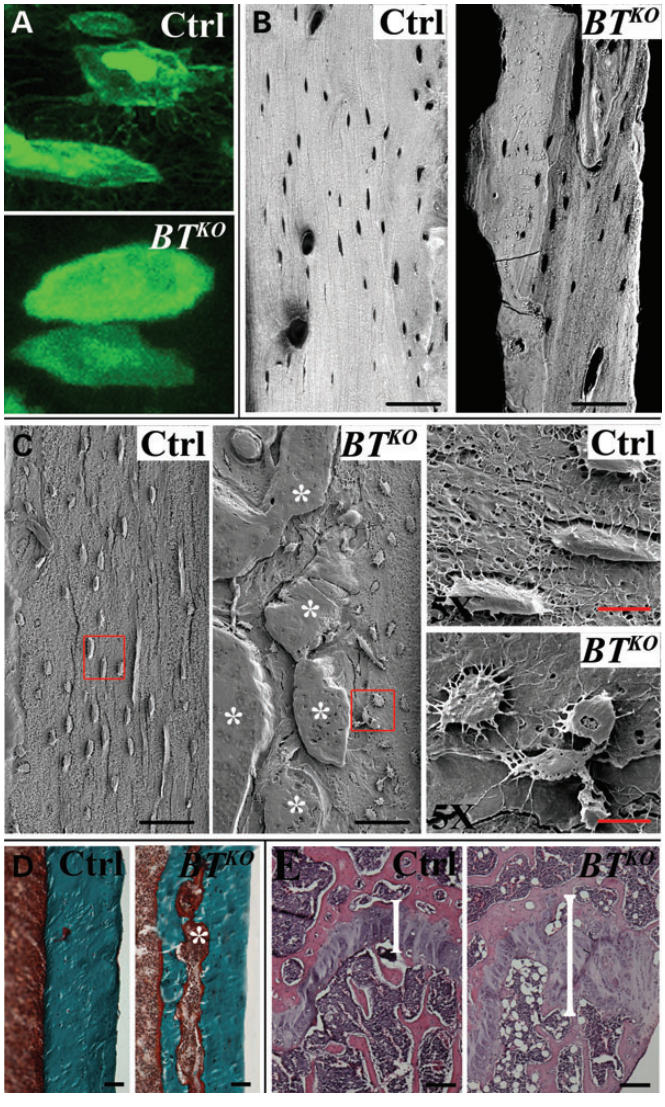

Figure 7. Morphological/structural defects in BT^{KO} bone. (**A**) A representative high-magnification comparison is shown for FITC staining of cortical areas of femur that shows BT^{KO} osteocytes (bottom panel) to have reduced numbers of dendritic processes than control osteocytes (top panel). (**B**) Representative backscattered SEM images contrast the homogeneous distribution of mineral in control cortical areas of femur with a heterogeneous distribution of areas of higher (white) and lower (grayish zones) levels of mineral in BT^{KO} femur and also shows BT^{KO} osteocytic lacunae to be fewer, generally more rounded and less spindle-shaped than in controls. (**C**) Illustrative acid-etched, resin-casted SEM images show in detail the malformed osteocytes and decreased numbers of dendrites in BT^{KO} cortical femur. Asterisks denote areas of osteoid. (**D**) Representative Goldner's Masson trichrome staining demonstrates the type of osteoid seam (asterisk) present in BT^{KO} cortical bone, but absent in controls. (**E**) H&E staining of femora shows BT^{KO} marrow to contain markedly more adipocytes than controls and shows BT^{KO} growth plates (brackets) to be relatively wider, compared with controls, and to have some disorganization in vertical columns. Black scale bars: 50 μm; red scale bar: 10 μm.

Molecular analyses of the BT^{KO} phenotype

The markedly reduced post-yield displacement of BT^{KO} femur, showing much reduced ductility, is diagnostic of the type of impaired collagen I properties that lead to brittle bones (i.e. OI). We have previously shown that BMP1, mTLD and mTLL1 are all capable of removing the procollagen I C-propeptide *in vitro* and that products of endogenous *Bmp1* and *Tll1* genes are together responsible for processing endogenous procollagen I C-propeptides in cultures of MEFs (10,23,24). To determine the extent to which *Bmp1* and *Tll1* ablation might affect procollagen

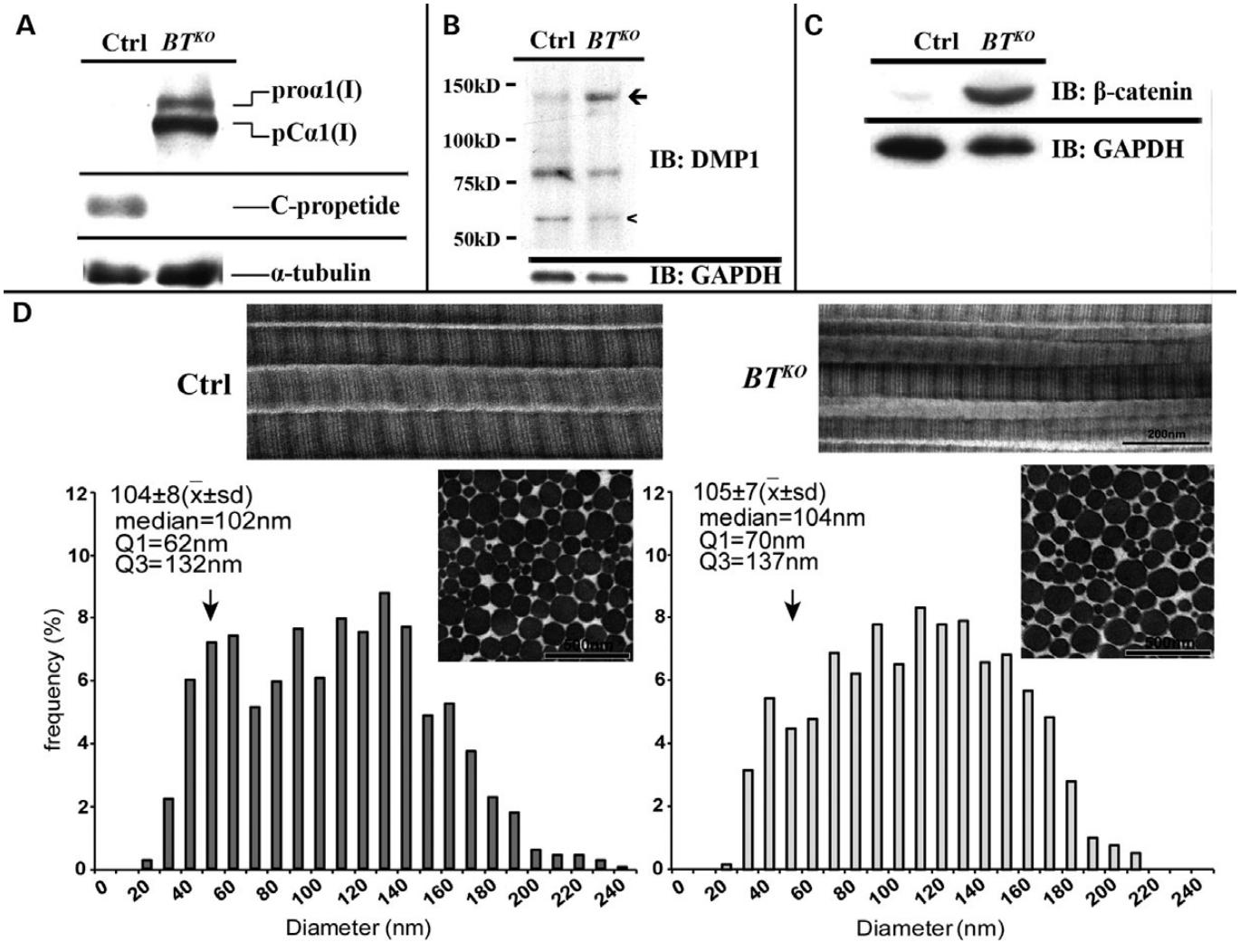

Figure 8. BT^{KO} bones show decreased processing of procollagen I and DMP1 and increased canonical Wnt signaling. Shown are western blots of extracts from femora of 17-week-old (**A** and **B**) and 10-week-old (**C**) BT^{KO} and control (Ctrl) mice. (A) Anti-procollagen I C-propeptide antibodies show decreased procollagen I processing in BT^{KO} femur. (B) Anti-DMP1 antibodies indicate a reduction in processing of DMP1 to its active 57-kDa form in BT^{KO} femur. (C) Anti-β-catenin antibodies provide evidence of higher canonical Wnt-signaling levels in BT^{KO} femur. All western blots were repeated using at least three different BT^{KO} and control samples, each from a different mouse. Representative images are shown. (**D**) TEM shows BT^{KO} tendon to have collagen fibrils that are grossly normal in appearance, but which have a shift in fibril diameter distributions to larger diameters. First quartile (Q1) values demonstrate a reduction in the small diameter subpopulation (vertical arrows) in BT^{KO} tendon, compared with control (62 nm versus 70 nm). In addition, the median, first quartile (Q1) and third quartile (Q3) values are all increased in the mutant tendon, indicating a general shift to larger diameter fibrils in BT^{KO} tendon. This increase in fibril diameter is consistent with the significant decrease in fibril density observed in BT^{KO} tendon relative to control (58/mm^2 versus 65/mm^2). X, mean; sd, standard deviation.

I processing in BT^{KO} bone, western blots of BT^{KO} and control femur extracts were probed with anti-procollagen I C-propeptide antibody. As can be seen from Figure 8A, procollagen C-propeptide cleavage is much reduced in BT^{KO} bone, although low levels of residual processing were observed upon overexposure of the blot (not shown). Surprisingly, although transmission electron microscopy (TEM) previously showed the collagen fibrils in $Bmp1^{-/-}$ (21) and $Bmp1^{-/-}/Tll1^{-/-}$ doubly null (23) embryos to have a 'barbed wire' appearance, with barb-like projections on fibril surfaces apparently associated with retained C-propeptides (36), TEM showed no discernable barbs associated with the collagen fibrils of BT^{KO} tendons (Fig. 8D) or bone (Supplementary Material, Fig. S5). In fact, measurement of tendon fibrils (measurements were made in tendon rather than bone, as the parallel fibrils of tendon greatly facilitates such measurements) found the only discernable difference to be a shift in BT^{KO} fibril diameter distributions to larger diameters, with a reduction in the subpopulation of less mature fibrils with diameters centered in the 50- to 55-nm range, a shift that may represent some loss of fine control in the lateral growth of collagen fibrils via lateral fusion of smaller diameter fibrils (Fig. 8D). In addition, there was a higher density of fibrils in control tendon than in BT^{KO} tendon, in which diameters were larger. No change in D-spacing was detected between BT^{KO} and control collagen fibrils.

A number of the defects observed in the BT^{KO} bone phenotype are reminiscent of defects seen in mice null for the DMP1 gene (*Dmp1*). Such defects include osteomalacia, shortened long bones with flared metaphyses, an abnormal osteocyte lacunocanalicular system and defective osteocyte maturation (17,37). As DMP1 has been proposed as a substrate for BMP1-like

proteinases (16), and as processing of DMP1 to produce active C-terminal 57-kDa fragment is necessary to DMP1 function (34,38), we determined whether such processing was actually impaired in BT^{KO} bone. As can be seen from Figure 8B, conversion of full-length ~120-kDa DMP1 to a 57-kDa C-terminal fragment is reduced in femur extracts of BT^{KO} femur, compared with control femur. Thus, it can be concluded that BMP1-like proteinases do participate in the *in vivo* processing/activation of DMP1 in bone. However, it is not clear from the western blots the extent to which DMP1 cleavage is reduced in BT^{KO} bone. It has previously been reported that *Dmp1*-null mice have malformed, expanded growth plates, in which the normally vertical columns of chondrocytes have become disorganized, and a dramatically expanded hypertrophic zone is observed (37). There does appear to be a relatively minor defect in BT^{KO} growth plates as documented by expanded cartilage zones, with mild disorganization in vertical columns (Fig. 7E), and the reduction of trabecular BV in the metaphysis (Fig. 6) is also suggestive of a deficit in endochondral bone formation. However, the growth plate defects are much milder than those in *Dmp1*-null mice. In addition, *Dmp1*-null mice are severely hypophosphatemic and mildly hypocalcemic (39), whereas there were no significant differences in serum phosphate (P_i: BT^{KO} 0.8749 $\pm$ 0.0494 mmol/ml, $n = 8$; control 0.8734 $\pm$ 0.0604 mmol/ml, $n = 8$) or serum ionized calcium (Ca^{2+}: BT^{KO} 7.741 $\pm$ 0.196 mg/dl, $n = 8$; control 7.793 $\pm$ 0.203 mg/dl, $n = 8$) between BT^{KO} and control mice. Thus, there appears to be sufficient residual DMP1 cleavage in BT^{KO} mice to avoid the full-blown growth plate and serum electrolyte phenotypes observed in *Dmp1*-null mice.

Although there have been no previous reports of the involvement of BMP1-like proteinases in the regulation of Wnt signaling, the observed decrease in BT^{KO} bone of staining for sclerostin (above), which is an inhibitor of Wnt signaling (40), and the recent importance that canonical Wnt signaling has been shown to play in bone modeling and mineral density (41), prompted us to determine whether levels of canonical Wnt signaling in BT^{KO} bone might differ from those of controls. Interestingly, consistent with the decreased sclerostin staining in BT^{KO} femora (Fig. 7F), the femora of 10-week-old BT^{KO} mice showed marked increases in the levels of β-catenin (Fig. 8C), indicative of marked increases in the levels of canonical Wnt signaling.

DISCUSSION

Here, we present novel, floxed *Bmp1* and *Tll1* mouse strains that have enabled us to overcome the barriers of $Bmp1^{-/-}$ and $Tll1^{-/-}$ lethality and issues of functional redundancy, to begin in-depth characterization of *in vivo* functions of a family of proteinases hypothesized to play key roles in vertebrate development and homeostasis and, in particular, in ECM formation and maintenance (4,5). The association of mutations that disrupt procollagen I C-propeptide processing with cases of dominant OI (11) and recent association of BMP1 amino acid changes with cases of recessive OI (12,13) prompted us to focus initial analysis of BT^{KO} mice on the skeletal system.

Three-point bending analysis showed BT^{KO} bone to be markedly weak and brittle, the definitive characteristics of OI. In particular, impaired post-yield deformation, or ductility, implied an ECM protein defect, consistent with the possibility that the BT^{KO} bone phenotype is, like cases of OI (1–3), impacted by deficits in the formation and/or properties of collagen I fibrils, as such fibrils are thought to provide most of the tensile strength of bone. As is also the case in OI, at least some of the mineralization defects in BT^{KO} bone are presumed to arise secondarily to deficits in collagen I fibrils, which are thought to be intimately involved in the nucleation and growth of the nanocrystals that constitute bone mineralization (42). Dynamic histomorphometry results and the markedly increased levels of active osteoblasts and osteoclasts at mineralizing surfaces in BT^{KO} bone are all consistent with a model in which BT^{KO} osteoblasts deposit an inferior quality ECM, resulting in dramatically increased bone turnover in an ultimately futile attempt to repair/replace the inferior bone.

Despite the ECM defect implied by mechanical testing, and the pronounced deficit in procollagen C-propeptide cleavage, BT^{KO} collagen fibrils were surprisingly normal in appearance via TEM, with the only obvious morphological abnormality being a shift to larger fibril diameter distributions, perhaps representing some loss of fine control in collagen fibril lateral growth. In contrast, TEM has shown *Bmp1*-null (21) and $Bmp1^{-/-}Tll1^{-/-}$ doubly null (23) embryos to have distinctly abnormal collagen fibrils with barb-like projections, demonstrated by immunohistochemistry to be associated with retained C-propeptides (36). It is possible that morphological defects in BT^{KO} collagen fibrils would be more pronounced if tamoxifen-induced excision of *Bmp1*/*Tll1* sequences was pre- rather than post-natal. However, TEM examination of dermal collagen fibrils of OI patients with C-propeptide cleavage site mutations also showed a lack of barbs (11) (collagen fibrils of OI patients with BMP1 missense mutations (12,13) have yet to be characterized via TEM). We thus suggest that C-propeptide-associated barbs may become detectable via TEM only when C-propeptide processing activity falls below some threshold. This suggests that C-propeptide processing activity is lower in *Bmp1*-null embryos than that in BT^{KO} tissues, which is plausible, as *Bmp1* function is totally absent in the former, but low residual *Bmp1* expression remains in the latter, and, although *Tll1* expression is much reduced in BT^{KO} tissues, *Bmp1* may provide higher levels of *in vivo* pCP activity than does *Tll1* (22). It is also possible that the appearance of barbs on $Bmp1^{-/-}$ embryo fibrils and their absence on fibrils of BT^{KO} mice or OI patients with C-propeptide processing defects may be influenced by differences in embryonic and postnatal processes of collagen fibrillogenesis, which have been documented in some tissues (43). Future experiments, involving use of $Bmp1^{floxed}/^{-}$ mice, compound heterozygous for floxed and null *Bmp1* alleles (thus providing lower levels of residual *Bmp1* activity upon tamoxifen treatment than those found in BT^{KO} mice) and both pre- and post-natal ablation of *Bmp1* activity, will provide additional insights into how levels of pCP activity and pre- and post-natal mechanisms of fibrillogenesis may contribute to formation of C-propeptide-associated barbs on collagen fibrils.

Although dermal collagen fibrils of OI patients with C-propeptide cleavage site mutations were reported to have irregular profiles with 'blebs' on fibril surfaces, upon cross section (11), such irregular cross sections with blebs were not detected in BT^{KO} fibrils, and thus do not appear to be consistent

features of fibrils in tissues with lowered C-propeptide processing levels.

Analysis by μ-CT showed BT^{KO} bones to have a generalized decrease in mineral density, although backscattered SEM showed mineral to be heterogeneously distributed, with areas of low and high density. In contrast, a generalized increase in bone mineral density was reported for the two mild OI patients with C-propeptide cleavage site mutations and for a sib pair with mild OI and a *BMP1* signal peptide missense mutation that impairs secretion (11,12). A generalized increase in bone mineral density was also reported for zebrafish with mutations in the BMP1 gene *bmp1a* (12). However, despite the apparent contrast between generalized decreases and increases in mineral density in BT^{KO} bones and these other skeletal phenotypes, respectively, a feature at least some of these reported phenotypes share with the BT^{KO} phenotype is heterogeneity in the distribution of bone mineral. In the zebrafish model, for example, although adult vertebrae had increased mineral density, mineral density was reduced in fin bones and in larval vertebrae (12). In the OI patients with C-propeptide cleavage mutations, although DXA analysis indicated elevated bone mineral density and Fourier transform infrared imaging showed an increased mineral/ECM ratio, both patients had radiographic osteopenia, and pronounced heterogeneity of mineralization was documented in one of the patients (11). Importantly, a sib pair with a *BMP1* protease domain missense mutation and a severe OI-like phenotype was, like BT^{KO} mice, reported to have generalized decreases in bone density (distribution of mineral was not analyzed) (13). We interpret these various observations to mean that diminished BMP1-like proteinase activity, or even just a deficit in the levels of C-propeptide cleavage, leads to deranged ECM–mineral interactions that can have varying effects on mineral deposition, leading to heterogeneity in mineral density not only between different skeletal phenotypes but also within a given bone. Variables that affect whether mineral levels will be increased or decreased in a given context by these types of mutations remain to be determined.

Proteolytic cleavage of DMP1 is reduced in BT^{KO} bone, consistent with the osteomalacia, shortened long bones with flared metaphyses, enlarged entheses, abnormal osteocyte lacunocanalicular system and defective osteocyte morphology/maturation seen in these bones, all of which defects have been described in $Dmp1^{-/-}$ mice and in human patients with autosomal recessive hypophosphatemic rickets caused by mutations in the *DMP1* gene (17). However, unlike $Dmp1^{-/-}$ mice, which have rickets, grossly broadened and deranged growth plates and are severely hypophosphatemic, BT^{KO} mice are not rachitic and have relatively minor growth plate defects and normal serum phosphate levels. Interestingly, both rickets and growth plate defects in $Dmp1^{-/-}$ mice are secondary to hypophosphatemia, whereas osteomalacia is, for the most part, not (17). We thus speculate that sufficient DMP1 is activated by residual *Bmp1* and/or *Tll1* expression in BT^{KO} mice to avoid hypophosphatemia and attendant major growth plate defects and rickets, whereas the diminution in proteolytic activation of DMP1 is sufficient to contribute to the mineralization defects and derangements in osteocytic biology seen in these mice—derangements that appear to contribute in a substantial way to the BT^{KO} skeletal phenotype.

Although BT^{KO} and $Dmp1^{-/-}$ bone are similar in having increased numbers of AP-positive osteoblasts, they differ in that BT^{KO} bone has increased, whereas $Dmp1^{-/-}$ bone has decreased numbers of TRAP-positive osteoclasts (44). The reduced numbers of osteoclasts in $Dmp1^{-/-}$ bone may be, to some extent, a secondary effect of hypophosphatemia (44), which does not occur in BT^{KO} mice, whereas the increased numbers of osteoclasts in BT^{KO} bone may be influenced, to some degree, by the abnormal collagen of BT^{KO} bone, as defective bone collagen has been suggested to contribute to elevation of osteoclast levels in OI (45). The extent to which reduced cleavage of proposed substrates of BMP1-like proteinases other than DMP1 and procollagen I might contribute to the BT^{KO} skeletal phenotype remains to be determined.

Interestingly, and consistent with decreased staining in BT^{KO} femora for sclerostin, a marker for mature osteocytes and an inhibitor of canonical Wnt signaling, femora of 10-week-old BT^{KO} mice showed markedly increased β-catenin levels, indicative of markedly increased canonical Wnt signaling. This result may seem counterintuitive, as increased canonical Wnt signaling has previously been associated, by numerous studies, with increased bone mass and strength (41), and as both of the latter are reduced in BT^{KO} mice. Nevertheless, we surmise that the lower sclerostin levels, resulting from deficits in osteocyte maturation, result in increased canonical Wnt signaling that helps drive the increased numbers of active osteoblastic cells involved in the accelerated bone remodeling observed in BT^{KO} bone. In addition, it is thought that bone bending in response to strain results in decreased sclerostin expression by osteocytes, thus locally increasing Wnt signaling to increase bone mass as part of the adaptive response of bone to strain (46,47). Because the BT^{KO} bones are less stiff than the control bones, the BT^{KO} bones would experience more strain in response to a given load than would control bones, and this might be expected to contribute to decreased sclerostin production, except in cases where the maturation deficits of BT^{KO} osteocytes compromise their usual role as mechanosensors (48). The observation of high Wnt signaling in BT^{KO} bone is germane to current efforts to develop new bone-building therapies for increasing bone mass via positively modulating canonical Wnt signaling (41), as they demonstrate an example of low bone mass and high bone fragility in which canonical Wnt signaling is already at high levels, such that up-modulation of such signaling might not be expected to effectively ameliorate the bone phenotype. Such therapies can be tested in the BT^{KO} mouse, to determine whether this is the case.

Wnt signaling is thought to favor the differentiation of mesenchymal stem cells (MSCs) down the osteoblastic, rather than the adipocytic, pathway (49), consistent with the increased numbers of active osteoblasts observed in BT^{KO} bone. In this context, however, it was surprising that BT^{KO} bone also contained markedly more adipocytes than did control bones (e.g. Fig. 7E). We note that BMP1-like proteinases are thought to be involved in regulating a number of signaling pathways (e.g. BMP signaling) (4) that can interact with the Wnt-signaling pathway in complex ways to affect MSC differentiation (49). Moreover, as interactions with ECM components doubtless affect MSC differentiation, deficits in processing of various ECM components in BT^{KO} bone may contribute to the abnormal distribution/numbers of cell types seen in this tissue. Future experiments employing cultures containing BT^{KO} and control bone MSCs will attempt to identify the factors involved in producing the

abnormal distribution/numbers of MSC-derived cell types found in BT^{KO} bone.

It has been reported that human and rat plasma contain mTLD (50), one of the two alternatively spliced proteinases encoded by the gene that also encodes BMP1, and that i.v. injection of recombinant mTLD or anti-mTLD antibody enhances or delays, respectively, bone fracture repair in rats (28). Clearly, the BT^{KO} mouse model system presented here provides the opportunity for determining the extent to which circulating mTLD may normally affect bone growth and modeling, via injecting recombinant mTLD into BT^{KO} mice and determining the extent to which this may ameliorate the bone phenotype. Such studies could provide a direct readout of the portion of the BT^{KO} bone phenotype owing to loss of circulating mTLD and would also provide insights into the potential for therapeutic interventions via administrating exogenous BMP1-like proteinases to OI patients with deficiencies in endogenous BMP1-like proteinases (12,13), or C-propeptide cleavage site mutations that delay procollagen processing (11,51). Comparable studies could employ recombinant BMP1 and mTLL1, or cocktails comprising combinations of the three proteinases, to determine the most efficacious therapeutic approach.

MATERIALS AND METHODS

Tll1- and *Bmp1*-floxed mice

129/Sv genomic DNA from the 5′ homology arm of a previously described *Tll1* targeting vector (22) was cleaved with BglII, partially filled with dATP and dGTP, and recut with Xba I to produce a 759-bp fragment containing exon VI. This fragment was ligated into vector ploxPNT (52,53), which had been cut with SalI, partially filled with dCTP and dTTP, and then recut with XbaI. In resulting plasmid, ploxPNTVI, *Tll1* exon VI replaced the *neo*^{r} cassette of the original ploxPNT vector, as an insert flanked by *loxP* sites. A 3.2-kb EcoRI-XbaI genomic fragment previously used as a *Tll1* 5′ homology arm (22) was placed into pBluescript II KS+ (Stratagene), and the resulting plasmid was cut with KpnI and ClaI, removing the pBluescript polylinker ClaI site, but retaining the polylinker KpnI site, now fused to the 5′ end of the genomic insert. Oligomers 5′ CTA GACTGCAGAATCGATGC 3′ and 5′ GGCCGCATCGATT CTGCAGT 3′ were annealed to form a linker that was ligated to the 3′ end of the 3.2-kb insert to introduce PstI and ClaI sites. The modified insert was then excised with KpnI and ClaI and ligated into ploxPNTVI, which had been cut with KpnI-ClaI. The resulting plasmid was cut with XhoI and NotI, and the *Tll1* 3.6-kb 3′ homology arm described in Clark *et al*. (22) was inserted to produce plox*Tll1*. The latter was cut with NheI and treated with calf intestine AP. Plasmid J35 (54) was cut with EagI, self-ligated, partially digested with BamHI and then recut with BagI and BglII, to remove sequences flanked by the *frt* sites. The remaining vector backbone was then ligated to the Pgk1 promoter-*neo*^{r} cassette that had been cut from vector pPNT (52) with BamHI and NotI. The resulting plasmid, containing an *frt*-flanked *neo*^{r} cassette, was cut with NotI and blunt-ended with Klenow fragment (to remove a NotI site between the *neo*^{r} cassette and one of the *frt* sites that would have interfered with linearization of the final targeting vector) and then self-ligated to form plasmid pJFRTneo. Plasmid pJFRTneo was cut with BssHII and NcoI and ligated to a fragment formed via annealing of oligonucleotides 5′ CGCGCATG CCCGACGGCGAAGATCTCGTCGTGACC 3′ and 5′ CATG GGTCACGACGAGATCTTCGCCGTCGGGCATG 3′, which corrected an Asp to Glu mutation in the original pPNT *neo*^{r} cassette. The resulting plasmid was then cut with NheI, to release the *frt*-flanked *neo*^{r} cassette, which was then ligated into an NheI site of plox*Tll1* to form the finished targeting vector (Fig. 1A).

129/S6 embryonic stem (ES) cells were electroporated with NotI-linearized targeting vector and subjected to selection in G418 and gancyclovir, producing 287 doubly resistant colonies. Four correctly targeted lines were identified by Southern blotting (Fig. 1B). ES cells from the four independently targeted cell lines were injected into C57BL/6 blastocysts at the University of Wisconsin Biotechnology Center Transgenic mouse facility. Chimeras were crossed with C57BL/6 mice (Jackson Laboratories), and analysis of agouti offspring by Southern blotting for the targeted allele found germ line transmission from two of the independently targeted ES cell lines, leading to establishment of two separate mouse lines with allele $Tll1^{loxP-frt}$. For excision of the Pgk1 promoter-*neo*^{r} cassette, to produce allele $Tll1^{loxP}$, $Tll1^{loxP-frt}$ mice were crossed with the ACTB:FLPe line (55).

Generation of the *Bmp1*-floxed mice will be described elsewhere.

All mice were housed and treated in accordance with NIH guidelines, using protocols approved by the Research Animal Resources Center of the University of Wisconsin-Madison.

Induced excision of *Bmp1* and *Tll1* in juvenile mice

To excise floxed *Bmp1* and *Tll1* sequences, a mouse carrying the *Cre-ERT2* transgene under control of the human ubiquitin C promoter (29) was crossed onto a $Bmp1^{flox/flox}$; $Tll1^{flox/flox}$ background, to produce $Bmp1^{flox/flox}$; $Tll1^{flox/flox}$; *Cre-ERT2* mice. $Bmp1^{flox/flox}$; $Tll1^{flox/flox}$ littermate mice lacking the Cre transgene were used as controls in this study. Tamoxifen (Sigma Life Science) was administered to both $Bmp1^{flox/flox}$; $Tll1^{flox/flox}$; *Cre-ERT2* mice and $Bmp1^{flox/flox}$; $Tll1^{flox/flox}$ controls through IP injection at a concentration of 100 mg/kg body weight (solubilized in 98% corn oil, 2% ethanol) once per day for 6 days at 4 weeks and then again for 6 days at 6 weeks of age. $Bmp1^{flox/flox}$; $Tll1^{flox/flox}$; *Cre-ERT2* mice from which floxed sequences have been excised consequent to treatment with tamoxifen are hereafter referred to as BT^{KO} mice. Mice, unless otherwise indicated in the text, were sacrificed at 17 weeks of age for analysis.

Preparation and staining of whole skeletons

To obtain a global view of skeletal abnormalities, soft tissues were removed from intact skeletons using Dermestid beetles, at the University of Wisconsin-Madison Zoological Museum. Rib fractures were verified through alizarin red/alcian blue staining of whole mouse skeletons, as described previously (56). Briefly, mouse skeletons were eviscerated and fixed in 95% ethanol overnight. The preparations were then stained 3 days in alizarin red/alcian blue and then cleared through sequential incubations in 2% KOH, 25% glycerol/2% KOH, 50% glycerol/2% KOH, 75% glycerol/2% KOH and 100% glycerol.

Biomechanical testing

Femora were harvested from 10 BT^{KO} and 13 control males, and from 10 each BT^{KO} and control females. After sacrifice, femora were disarticulated and soft tissues were removed. Biomechanical performance of femoral diaphyses was tested using quasi-static three-point bending under displacement control with a support span of 7.5 mm, as previously described (57). Bones were loaded at a constant rate of 0.3 mm/sec until failure occurred. Both femora from each animal were tested, and the averaged value taken as the femoral biomechanical performance for that mouse. Geometric properties of the femora tested were obtained from analysis (SigmaScan) of digital images of the fracture cross section, and this information, along with the whole bone mechanical testing data obtained from the three-point bending experiment, was used to calculate material properties of the bone tissue according to standard beam theory equations (32,33).

X-ray radiography and high-resolution microcomputed tomography

Bones were dissected free of skeletal muscles for radiography with a Faxitron MX-20 specimen radiography system (Faxitron X-ray Corp.) as described previously (37). For high-resolution microcomputed tomography (μ-CT) analyses, femora were scanned at 3.5-μm resolution using a μ-CT35 imaging system (Scanco Medical). The μ-CT analyses included: (1) high-resolution scanning of the femur mid-shaft region (100 slices along the mid-shaft between the two epiphyses along the cranial–caudal axis and (2) high-resolution scanning of the femur metaphyseal region proximal to the distal growth plate for trabecular bone evaluations. In trabecular bone evaluations, 400 slices were chosen in the bone center, with the cortical shell excluded. Data obtained from high-resolution μ-CT scanning were analyzed via Scanco software, which provided: the bone volume-to-total volume ratio (BV/TV), Tb.N, trabecular thickness (Tb.Th), trabecular spacing (Tb.Sp) and tissue mineral density.

Dynamic and cellular histomorphometry of bones

To prepare bone samples for histomorphometric analysis, mice received intraperitoneal injections of 10 mg/kg calcein (Sigma C-0875) and 30 mg/kg alizarin complexone (Sigma A-3882) at 7 and 2 days, respectively, prior to sacrifice, at 17 weeks of age. Whole hindlimbs were dissected from the hip, and skin and non-adherent muscle and connective tissues were removed from the bone, without scraping periosteal surfaces. Proximal femur and distal tibial bone was then removed to expose the marrow space, and the bone samples, with knee joints intact, were placed in 10% formalin at 4°C for 2–3 days with slow agitation. Samples were then subjected to computer-automated dynamic and cellular bone histomorphometry, essentially as described by Hong *et al*. (58).

Histology

Bones were fixed in 10% formalin at 4°C, decalcified and embedded in paraffin, and 4-μm-thick sections were used for H&E and TRAP staining, and immunohistochemistry, as described previously (17). For immunohistochemical analyses, the following antibodies were used: anti-MEPE (59) (gift from Larry Fisher, National Institutes of Health, Bethesda, MD, USA), diluted 1:400; anti-sclerostin (R&D Biosystems), diluted 1:400; and anti-E-11 [(60), gift from Lynda Bonewald], diluted 1:50, polyclonal antibodies. Un-demineralized specimens were embedded in methylmethacrylate, and 6 μm sections were subjected to Goldner's Masson trichrome staining, as previously described (17).

Backscattered scanning electron microscopy, acid etching SEM and FITC imaging

Long bones were dissected and fixed in 70% ethanol at room temperature for 24 h. Tissue specimens were then dehydrated in ascending concentrations of ethanol (from 70 to 100%), embedded in MMA without decalcification and sectioned using a water-cooled diamond-impregnated circular saw (Isomet, Buehler). The cut surface was polished using 1-, 0.3- and 0.05-μm alumina alpha micropolish II solutions (Buehler) on a soft cloth rotating wheel (61). Each sample was placed in an ultrasonic bath between steps and immediately following the polishing steps. The dehydrated specimens were then sputter-coated with carbon and scanned with a backscattered electron detector in a JEOL JSM-6010LA scanning electron microscope. Parameters were kept constant while the backscattered SEM images were taken under the scanning electron microscope, as described previously (17,62).

Staining with FITC (fluorescein isothiocyanate) was performed essentially as described (63,64). Briefly, long bones, immediately after harvesting and dissection, were placed in 10% formalin at 4°C for 2 days, followed by embedding in MMA bone blocks. A cross section (1–2 mm thick) was cut with a diamond-bladed saw (Buehler), and the cortical sections were then sanded and ground to a final thickness of ~100 μm for confocal imaging.

Western blot analysis

Disarticulated femora, with soft tissue removed, were frozen and homogenized to a fine powder in liquid nitrogen, using a porcelain mortar and pestle. The powder was then transferred into T-PER Tissue Protein Extraction Reagent with Halt protease inhibitor (Thermo Scientific). Samples were then sonicated 30 s and centrifuged, and supernatants were stored at −80°C until use; at which time, 50 μg aliquots/lane were subjected to SDS–PAGE and then transferred to nitrocellulose filters (one DMP1 western blot in Figure 8B was transferred to PVDF membrane), which were then blocked in 5% nonfat dry milk. Blots were probed with polyclonal antibody LF-41, directed against the pro-α1(I) C-propeptide (65), a gift from Larry Fisher; rabbit polyclonal antibody 857, specific for the C-terminal region of DMP1 (66), the kind gift of Chunlin Qin (Baylor College of Dentistry, Dallas, TX, USA); mouse monoclonal antibody against mouse β-catenin (BD Biosciences), rabbit polyclonal GAPDH (Sigma) and mouse monoclonal antibody to α-tubulin (Millipore). Secondary anti-rabbit and anti-mouse IgG antibodies both were from BioRad. Primary and secondary antibodies were diluted 1:1000 and 1:5000, respectively. Procollagen and α-tubulin blots, and the DMP1 blot on PVDF

membrane, were visualized using the ECL kit, whereas all other blots were visualized using the ECL Plus kit (both kits were from GE Healthcare). All western blots were repeated using at least 3 different BT^{KO} and control samples, each from a different mouse. Representative images are shown.

Transmission electron microscopy

Achilles tendons were fixed in 4% paraformaldehyde, 2.5% glutaraldehyde, 0.1 M sodium cacodylate and 8 mM $CaCl_2$, adjusted to pH 7.4 with NaOH. After 15 min at room temperature, fixation continued at 4°C for 2 h, followed by transfer to buffer containing 0.4% paraformaldehyde, 0.25% glutaraldehyde, 10% sucrose and 0.1 M sodium cacodylate at 4°C. Tendons were then rinsed with cacodylate buffer and post-fixed 1 h with 1% osmium tetroxide, dehydrated in an ethanol series followed by 100% propylene oxide, infiltrated and embedded in a mixture of Embed 812, nadic methyl anhydride, dodecenylsuccinic anhydride and DMP-30 (EM Sciences) and polymerized overnight at 60°C. Ultra-thin, ~90 nm sections were prepared using a Leica ultramicrotome and post-stained with 2% aqueous uranyl acetate and 1% phosphotungstic acid, pH 3.2. Sections were examined and imaged at 80 kV using a JEOL 1400 transmission electron microscope equipped with a Gatan Orius widefield side mount CC Digital camera. Bone was processed similarly, except that after fixation specimens were rinsed with cacodylate buffer and transferred to decalcification solution (10% EDTA in PBS, pH 7.4), containing 0.4% paraformaldehyde and 0.25 glutaraldehyde on a rocker at 4°C. Decalcification solution was changed every 2–3 days for 12 days.

Tendon diameter analysis was obtained from pooled data from one tendon from each of three mice of same genotype. Five or ten digital images from each tendon were taken from non-overlapping areas at ×50 000. Images were randomized and masked before fibril diameters were measured using a RM Biometrics-Bioquant Image Analysis System. A region of interest (ROI) of appropriate size was determined within the image so that a minimum of 60 fibrils were measured from each image. All fibrils in the ROI were measured per image. Fibril diameters were measured along the minor axis of the fibril cross section. Tendon diameter measurements were pooled into groups by genotype.

Reverse transcription PCR for detected excision of Bmp1 and Tll1 sequences

Disarticulated femora, soft tissue- and marrow-free, were frozen and homogenized to a fine powder in liquid nitrogen, using a porcelain mortar and pestle. RNA was extracted from the powder using TRIzol reagent (Life Sciences Technology). Reverse transcription (RT)–PCR was performed using primers for *Tll1* (5′ CAGAGAGCCATGTTCAAGCA 3′, forward; and 5′ CTTGCA GGGTTTCTCCACAT 3′, reverse) and*Bmp1* (5′ TGGATGAG GAGGACTTGAGG 3′, forward; and 5′ GTGCTGTCTTGG AGGGTCTC 3′, reverse).

Serum biochemistry

Serum calcium was measured in 17-week-old male mice using a colorimetric calcium kit (Pointe Scientific, Inc.) following the manufacturer's instructions. Serum inorganic phosphorus was measured in 17-week-old male mice by the ammonium molybdate–ascorbic acid method of Chen *et al.* (67).

Statistical analysis

Where appropriate, data were analyzed using Fischer's *t*-test and $P < 0.05$ was considered significant. All data are recorded as average ± SEM. For mechanical testing, as well as length measurements, left and right femora of each mouse were analyzed separately and the values averaged.

SUPPLEMENTARY MATERIAL

Supplementary Material is available at *HMG* online.

ACKNOWLEDGEMENTS

We thank Laura Halverson Monahan of the University of Wisconsin-Madison Zoological Museum for her assistance in the preparation of skeletons using Dermestid beetles, and the laboratory of Ray Vanderby, of the Department of Orthopedics and Rehabilitation, for access to and assistance with their three-point bending apparatus.

Conflict of Interest statement. None declared.

FUNDING

This work was supported by grants AR60636 and AR59685 (to S.-J.L.), AR54753 (to R.D.B.), AR44745 (to D.E.B.), DE018486 (to J.F.), and AR53815 and AR47746 (to D.S.G.) from the National Institutes of Health.

REFERENCES

1. Sillence, D.O., Senn, A. and Danks, D.M. (1979) Genetic heterogeneity in osteogenesis imperfecta. *J. Med. Genet.*, **16**, 101–116.
2. Byers, P.H. and Pyott, S.M. (2012) Recessively inherited forms of osteogenesis imperfecta. *Annu. Rev. Genet.*, **46**, 475–497.
3. Forlino, A., Cabral, W.A., Barnes, A.M. and Marini, J.C. (2011) New perspectives on osteogenesis imperfecta. *Nat. Rev. Endocrinol.*, **7**, 540–557.
4. Muir, A. and Greenspan, D.S. (2011) Metalloproteinases in Drosophila to humans that are central players in developmental processes. *J. Biol. Chem.*, **286**, 41905–41911.
5. Hopkins, D.R., Keles, S. and Greenspan, D.S. (2007) The bone morphogenetic protein 1/Tolloid-like metalloproteinases. *Matrix Biol.*, **26**, 508–523.
6. Wozney, J.M., Rosen, V., Celeste, A.J., Mitsock, L.M., Whitters, M.J., Kriz, R.W., Hewick, R.M. and Wang, E.A. (1988) Novel regulators of bone formation: molecular clones and activities. *Science*, **242**, 1528–1534.
7. Piccolo, S., Agius, E., Lu, B., Goodman, S., Dale, L. and De Robertis, E.M. (1997) Cleavage of Chordin by Xolloid metalloprotease suggests a role for proteolytic processing in the regulation of Spemann organizer activity. *Cell*, **91**, 407–416.
8. Blader, P., Rastegar, S., Fischer, N. and Strahle, U. (1997) Cleavage of the BMP-4 antagonist chordin by zebrafish tolloid. *Science*, **278**, 1937–1940.
9. Jasuja, R., Voss, N., Ge, G., Hoffman, G.G., Lyman-Gingerich, J., Pelegri, F. and Greenspan, D.S. (2006) bmp1 and mini fin are functionally redundant in regulating formation of the zebrafish dorsoventral axis. *Mech. Dev.*, **123**, 548–558.
10. Kessler, E., Takahara, K., Biniaminov, L., Brusel, M. and Greenspan, D.S. (1996) Bone morphogenetic protein-1: the type I procollagen C-proteinase. *Science*, **271**, 360–362.

11. Lindahl, K., Barnes, A.M., Fratzl-Zelman, N., Whyte, M.P., Hefferan, T.E., Makareeva, E., Brusel, M., Yaszemski, M.J., Rubin, C.J., Kindmark, A. *et al.* (2011) COL1 C-propeptide cleavage site mutations cause high bone mass osteogenesis imperfecta. *Hum. Mutat.*, **32**, 598–609.
12. Asharani, P.V., Keupp, K., Semler, O., Wang, W., Li, Y., Thiele, H., Yigit, G., Pohl, E., Becker, J., Frommolt, P. *et al.* (2012) Attenuated BMP1 function compromises osteogenesis, leading to bone fragility in humans and zebrafish. *Am. J. Hum. Genet.*, **90**, 661–674.
13. Martinez-Glez, V., Valencia, M., Caparros-Martin, J.A., Aglan, M., Temtamy, S., Tenorio, J., Pulido, V., Lindert, U., Rohrbach, M., Eyre, D. *et al.* (2012) Identification of a mutation causing deficient BMP1/mTLD proteolytic activity in autosomal recessive osteogenesis imperfecta. *Hum. Mutat.*, **33**, 343–350.
14. Uzel, M.I., Scott, I.C., Babakhanlou-Chase, H., Palamakumbura, A.H., Pappano, W.N., Hong, H.H., Greenspan, D.S. and Trackman, P.C. (2001) Multiple bone morphogenetic protein 1-related mammalian metalloproteinases process pro-lysyl oxidase at the correct physiological site and control lysyl oxidase activation in mouse embryo fibroblast cultures. *J. Biol. Chem.*, **276**, 22537–22543.
15. Scott, I.C., Imamura, Y., Pappano, W.N., Troedel, J.M., Recklies, A.D., Roughley, P.J. and Greenspan, D.S. (2000) Bone morphogenetic protein-1 processes probiglycan. *J. Biol. Chem.*, **275**, 30504–30511.
16. Steiglitz, B.M., Ayala, M., Narayanan, K., George, A. and Greenspan, D.S. (2004) Bone morphogenetic protein-1/Tolloid-like proteinases process dentin matrix protein-1. *J. Biol. Chem.*, **279**, 980–986.
17. Feng, J.Q., Ward, L.M., Liu, S., Lu, Y., Xie, Y., Yuan, B., Yu, X., Rauch, F., Davis, S.I., Zhang, S. *et al.* (2006) Loss of DMP1 causes rickets and osteomalacia and identifies a role for osteocytes in mineral metabolism. *Nat. Genet.*, **38**, 1310–1315.
18. Ge, G. and Greenspan, D.S. (2006) BMP1 controls TGFbeta1 activation via cleavage of latent TGFbeta-binding protein. *J. Cell Biol.*, **175**, 111–120.
19. Bonewald, L.F. and Mundy, G.R. (1990) Role of transforming growth factor-beta in bone remodeling. *Clin. Orthop. Relat. Res.*, **250**, 261–276.
20. Erlebacher, A., Filvaroff, E.H., Ye, J.Q. and Derynck, R. (1998) Osteoblastic responses to TGF-beta during bone remodeling. *Mol. Biol. Cell*, **9**, 1903–1918.
21. Suzuki, N., Labosky, P.A., Furuta, Y., Hargett, L., Dunn, R., Fogo, A.B., Takahara, K., Peters, D.M., Greenspan, D.S. and Hogan, B.L. (1996) Failure of ventral body wall closure in mouse embryos lacking a procollagen C-proteinase encoded by Bmp1, a mammalian gene related to Drosophila tolloid. *Development*, **122**, 3587–3595.
22. Clark, T.G., Conway, S.J., Scott, I.C., Labosky, P.A., Winnier, G., Bundy, J., Hogan, B.L. and Greenspan, D.S. (1999) The mammalian Tolloid-like 1 gene, Tll1, is necessary for normal septation and positioning of the heart. *Development*, **126**, 2631–2642.
23. Pappano, W.N., Steiglitz, B.M., Scott, I.C., Keene, D.R. and Greenspan, D.S. (2003) Use of Bmp1/Tll1 doubly homozygous null mice and proteomics to identify and validate in vivo substrates of bone morphogenetic protein 1/tolloid-like metalloproteinases. *Mol. Cell Biol.*, **23**, 4428–4438.
24. Scott, I.C., Blitz, I.L., Pappano, W.N., Imamura, Y., Clark, T.G., Steiglitz, B.M., Thomas, C.L., Maas, S.A., Takahara, K., Cho, K.W. *et al.* (1999) Mammalian BMP-1/tolloid-related metalloproteinases, including novel family member mammalian Tolloid-like 2, have differential enzymatic activities and distributions of expression relevant to patterning and skeletogenesis. *Dev. Biol.*, **213**, 283–300.
25. Takahara, K., Lyons, G.E. and Greenspan, D.S. (1994) Bone morphogenetic protein-1 and a mammalian tolloid homologue (mTld) are encoded by alternatively spliced transcripts which are differentially expressed in some tissues. *J. Biol. Chem.*, **269**, 32572–32578.
26. Takahara, K., Brevard, R., Hoffman, G.G., Suzuki, N. and Greenspan, D.S. (1996) Characterization of a novel gene product (mammalian tolloid-like) with high sequence similarity to mammalian tolloid/bone morphogenetic protein-1. *Genomics*, **34**, 157–165.
27. Lee, S.J. (2008) Genetic analysis of the role of proteolysis in the activation of latent myostatin. *PLoS One*, **3**, e1628.
28. Grgurevic, L., Macek, B., Mercep, M., Jelic, M., Smoljanovic, T., Erjavec, I., Dumic-Cule, I., Prgomet, S., Durdevic, D., Vnuk, D. *et al.* (2011) Bone morphogenetic protein (BMP)1–3 enhances bone repair. *Biochem. Biophys Res. Commun.*, **408**, 25–31.
29. Ruzankina, Y., Pinzon-Guzman, C., Asare, A., Ong, T., Pontano, L., Cotsarelis, G., Zediak, V.P., Velez, M., Bhandoola, A. and Brown, E.J. (2007) Deletion of the developmentally essential gene ATR in adult mice leads to age-related phenotypes and stem cell loss. *Cell Stem Cell*, **1**, 113–126.
30. Wolfman, N.M., McPherron, A.C., Pappano, W.N., Davies, M.V., Song, K., Tomkinson, K.N., Wright, J.F., Zhao, L., Sebald, S.M., Greenspan, D.S. *et al.* (2003) Activation of latent myostatin by the BMP-1/tolloid family of metalloproteinases. *Proc. Natl. Acad. Sci. USA*, **100**, 15842–15846.
31. Hamrick, M.W., McPherron, A.C., Lovejoy, C.O. and Hudson, J. (2000) Femoral morphology and cross-sectional geometry of adult myostatin-deficient mice. *Bone*, **27**, 343–349.
32. Solverson, P., Murali, S.G., Litscher, S.J., Blank, R.D. and Ney, D.M. (2012) Low bone strength is a manifestation of phenylketonuria in mice and is attenuated by a glycomacropeptide diet. *PLoS One*, **7**, e45165.
33. Turner, C.H. and Burr, D.B. (1993) Basic biomechanical measurements of bone: a tutorial. *Bone*, **14**, 595–608.
34. Lu, Y., Yuan, B., Qin, C., Cao, Z., Xie, Y., Dallas, S.L., McKee, M.D., Drezner, M.K., Bonewald, L.F. and Feng, J.Q. (2011) The biological function of DMP-1 in osteocyte maturation is mediated by its 57-kDa C-terminal fragment. *J. Bone Miner. Res.*, **26**, 331–340.
35. Klein-Nulend, J., Bakker, A.D., Bacabac, R.G., Vatsa, A. and Weinbaum, S. (2013) Mechanosensation and transduction in osteocytes. *Bone*, **54**, 182–190.
36. Steiglitz, B.M., Kreider, J.M., Frankenburg, E.P., Pappano, W.N., Hoffman, G.G., Meganck, J.A., Liang, X., Hook, M., Birk, D.E., Goldstein, S.A. *et al.* (2006) Procollagen C proteinase enhancer 1 genes are important determinants of the mechanical properties and geometry of bone and the ultrastructure of connective tissues. *Mol. Cell Biol.*, **26**, 238–249.
37. Ye, L., Mishina, Y., Chen, D., Huang, H., Dallas, S.L., Dallas, M.R., Sivakumar, P., Kunieda, T., Tsutsui, T.W., Boskey, A. *et al.* (2005) Dmp1-deficient mice display severe defects in cartilage formation responsible for a chondrodysplasia-like phenotype. *J. Biol. Chem.*, **280**, 6197–6203.
38. Sun, Y., Prasad, M., Gao, T., Wang, X., Zhu, Q., D'Souza, R., Feng, J.Q. and Qin, C. (2010) Failure to process dentin matrix protein 1 (DMP1) into fragments leads to its loss of function in osteogenesis. *J. Biol. Chem.*, **285**, 31713–31722.
39. Ling, Y., Rios, H.F., Myers, E.R., Lu, Y., Feng, J.Q. and Boskey, A.L. (2005) DMP1 depletion decreases bone mineralization in vivo: an FTIR imaging analysis. *J. Bone Miner. Res.*, **20**, 2169–2177.
40. Li, X., Zhang, Y., Kang, H., Liu, W., Liu, P., Zhang, J., Harris, S.E. and Wu, D. (2005) Sclerostin binds to LRP5/6 and antagonizes canonical Wnt signaling. *J. Biol. Chem.*, **280**, 19883–19887.
41. Baron, R. and Kneissel, M. (2013) WNT signaling in bone homeostasis and disease: from human mutations to treatments. *Nat. Med.*, **19**, 179–192.
42. Eyre, D.R. and Weis, M.A. (2013) Bone collagen: new clues to its mineralization mechanism from recessive osteogenesis imperfecta. *Calcif Tissue Int.*, **93**, 338–347.
43. Canty, E.G., Lu, Y., Meadows, R.S., Shaw, M.K., Holmes, D.F. and Kadler, K.E. (2004) Coalignment of plasma membrane channels and protrusions (fibripositors) specifies the parallelism of tendon. *J. Cell Biol.*, **165**, 553–563.
44. Zhang, R., Lu, Y., Ye, L., Yuan, B., Yu, S., Qin, C., Xie, Y., Gao, T., Drezner, M.K., Bonewald, L.F. *et al.* (2011) Unique roles of phosphorus in endochondral bone formation and osteocyte maturation. *J. Bone Miner. Res.*, **26**, 1047–1056.
45. Uveges, T.E., Collin-Osdoby, P., Cabral, W.A., Ledgard, F., Goldberg, L., Bergwitz, C., Forlino, A., Osdoby, P., Gronowicz, G.A. and Marini, J.C. (2008) Cellular mechanism of decreased bone in Brtl mouse model of OI: imbalance of decreased osteoblast function and increased osteoclasts and their precursors. *J. Bone Miner. Res.*, **23**, 1983–1994.
46. Frost, H.M. (1987) Bone 'mass' and the 'mechanostat': a proposal. *Anat. Rec.*, **219**, 1–9.
47. Tu, X., Rhee, Y., Condon, K.W., Bivi, N., Allen, M.R., Dwyer, D., Stolina, M., Turner, C.H., Robling, A.G., Plotkin, L.I. *et al.* (2012) Sost downregulation and local Wnt signaling are required for the osteogenic response to mechanical loading. *Bone*, **50**, 209–217.
48. Bonewald, L.F. and Johnson, M.L. (2008) Osteocytes, mechanosensing and Wnt signaling. *Bone*, **42**, 606–615.
49. Lin, G.L. and Hankenson, K.D. (2011) Integration of BMP, Wnt, and notch signaling pathways in osteoblast differentiation. *J. Cell Biochem.*, **112**, 3491–3501.
50. Grgurevic, L., Macek, B., Healy, D.R., Brault, A.L., Erjavec, I., Cipcic, A., Grgurevic, I., Rogic, D., Galesic, K., Brkljacic, J. *et al.* (2011) Circulating

bone morphogenetic protein 1–3 isoform increases renal fibrosis. *J. Am. Soc. Nephrol.*, **22**, 681–692.
51. Pollitt, R., McMahon, R., Nunn, J., Bamford, R., Afifi, A., Bishop, N. and Dalton, A. (2006) Mutation analysis of COL1A1 and COL1A2 in patients diagnosed with osteogenesis imperfecta type I-IV. *Hum. Mutat.*, **27**, 716.
52. Tybulewicz, V.L., Crawford, C.E., Jackson, P.K., Bronson, R.T. and Mulligan, R.C. (1991) Neonatal lethality and lymphopenia in mice with a homozygous disruption of the c-abl proto-oncogene. *Cell*, **65**, 1153–1163.
53. Shalaby, F., Rossant, J., Yamaguchi, T.P., Gertsenstein, M., Wu, X.F., Breitman, M.L. and Schuh, A.C. (1995) Failure of blood-island formation and vasculogenesis in Flk-1-deficient mice. *Nature*, **376**, 62–66.
54. Struhl, G. and Basler, K. (1993) Organizing activity of wingless protein in Drosophila. *Cell*, **72**, 527–540.
55. Rodriguez, C.I., Buchholz, F., Galloway, J., Sequerra, R., Kasper, J., Ayala, R., Stewart, A.F. and Dymecki, S.M. (2000) High-efficiency deleter mice show that FLPe is an alternative to Cre-loxP. *Nat. Genet.*, **25**, 139–140.
56. McLeod, M.J. (1980) Differential staining of cartilage and bone in whole mouse fetuses by alcian blue and alizarin red S. *Teratology*, **22**, 299–301.
57. Saless, N., Litscher, S.J., Lopez Franco, G.E., Houlihan, M.J., Sudhakaran, S., Raheem, K.A., O'Neil, T.K., Vanderby, R., Demant, P. and Blank, R.D. (2009) Quantitative trait loci for biomechanical performance and femoral geometry in an intercross of recombinant congenic mice: restriction of the Bmd7 candidate interval. *FASEB J.*, **23**, 2142–2154.
58. Hong, S.H., Jiang, X., Chen, L., Josh, P., Shin, D.G. and Rowe, D. (2012) Computer-automated static, dynamic and cellular bone histomorphometry. *J. Tissue Sci. Eng.*, **S1**, 004.
59. Ogbureke, K.U. and Fisher, L.W. (2004) Expression of SIBLINGs and their partner MMPs in salivary glands. *J. Dent. Res.*, **83**, 664–670.
60. Zhang, K., Barragan-Adjemian, C., Ye, L., Kotha, S., Dallas, M., Lu, Y., Zhao, S., Harris, M., Harris, S.E., Feng, J.Q. *et al.* (2006) E11/gp38 selective expression in osteocytes: regulation by mechanical strain and role in dendrite elongation. *Mol. Cell Biol.*, **26**, 4539–4552.
61. Miller, S.C., Omura, T.H. and Smith, L.J. (1985) Changes in dentin appositional rates during pregnancy and lactation in rats. *J. Dent. Res.*, **64**, 1062–1064.
62. Martin, D.M., Hallsworth, A.S. and Buckley, T. (1978) A method for the study of internal spaces in hard tissue matrices by SEM, with special reference to dentine. *J. Microsc.*, **112**, 345–352.
63. Ascenzi, M.G. and Roe, A.K. (2012) The osteon: the micromechanical unit of compact bone. *Front. Biosci. (Landmark Ed)*, **17**, 1551–1581.
64. Cao, Z., Zhang, H., Zhou, X., Han, X., Ren, Y., Gao, T., Xiao, Y., de Crombrugghe, B., Somerman, M.J. and Feng, J.Q. (2012) Genetic evidence for the vital function of Osterix in cementogenesis. *J. Bone Miner. Res.*, **27**, 1080–1092.
65. Fisher, L.W., Stubbs, J.T. 3rd and Young, M.F. (1995) Antisera and cDNA probes to human and certain animal model bone matrix noncollagenous proteins. *Acta. Orthop. Scand. Suppl.*, **266**, 61–65.
66. Maciejewska, I., Cowan, C., Svoboda, K., Butler, W.T., D'Souza, R. and Qin, C. (2009) The NH2-terminal and COOH-terminal fragments of dentin matrix protein 1 (DMP1) localize differently in the compartments of dentin and growth plate of bone. *J. Histochem. Cytochem.*, **57**, 155–166.
67. Chen, P.S., Toribara, T.Y. and Warner, H. (1956) Microdetermination of phosphorus. *Anal. Chem.*, **28**, 1756–1758.